Available online at www.sciencedirect.com

SciVerse ScienceDirect

Geochimica et Cosmochimica Acta 104 (2013) 232–260

Geochimica et Cosmochimica Acta

www.elsevier.com/locate/gca

Experimentally determined mineral/melt partitioning of first-row transition elements (FRTE) during partial melting of peridotite at 3 GPa

Fred A. Davis [a,*], Munir Humayun [b], Marc M. Hirschmann [a], Rupert S. Cooper [a]

[a] Department of Earth Sciences, University of Minnesota, 108 Pillsbury Hall, Minneapolis, MN 55455, USA
[b] Department of Earth, Ocean, & Atmospheric Science, and National High Magnetic Field Laboratory, Florida State University, Tallahassee, FL 32310-4100, USA

Received 11 July 2012; accepted in revised form 2 November 2012; Available online 29 November 2012

Abstract

Ratios of first-row transition elements (FRTE), such as Fe/Mn and Zn/Fe, may be fractionated differently by partial melting of peridotite than by partial melting of recycled lithologies like eclogite, and therefore may be useful as indicators of the source lithologies of mantle-derived basalts. Interpretation of basalt source lithologies from FRTE ratios requires accurate assessment of FRTE partitioning behavior between peridotitic minerals and coexisting melts. We present experimental determinations of partition coefficients for several of the FRTE (Sc, Ti, V, Cr, Mn, Fe, Co, Zn) and Ga and Ge between basaltic melt and olivine, garnet, pyroxenes, and spinel at 3 GPa. Because mineral/melt partitioning is sensitive to phase compositions, a key feature of these experiments is that the melts and minerals are known from previous experiments to be in equilibrium at the solidus of garnet peridotite at 3 GPa. Therefore, these partition coefficients are directly applicable to near-solidus partial melting of the mantle at 3 GPa. We use these partition coefficients to calculate compositions of model partial melts of peridotite and compare these to natural OIB. Model partial melts of peridotite have lower Fe/Mn (<62) and higher Co/Fe ($>7 * 10^{-4}$) than many primitive OIB, which implies that some other source lithology participates in the formation of many OIB. Alternatively, these ratios may potentially be produced by garnet peridotite if the source contains $\sim$0.3% Fe_2O_3, consistent with observations from continental xenoliths. Zn/Fe is a less sensitive indicator of non-peridotite source lithology than either Fe/Mn or Co/Fe, as Zn/Fe in partial melts of peridotite overlaps with >75% of primitive OIB. Ga and Sc are fractionated significantly by residual garnet, and high Ga/Sc may indicate the presence of garnet in basalt source regions. When taking into account several FRTE ratios simultaneously, few OIB appear to be consistent with derivation solely from a reduced peridotitic source. The source either must have a modest non-peridotitic component, be Fe-enriched, or be slightly oxidized.
© 2012 Elsevier Ltd. All rights reserved.

1. INTRODUCTION

Variations in radiogenic isotope ratios in mantle-derived basalts demonstrate that Earth's mantle is chemically heterogeneous (e.g., Zindler and Hart, 1986). These variations in isotopic signatures have been correlated with major and minor element variations of primitive oceanic basalts (Hauri, 1996; Kogiso et al., 1997; Jackson and Dasgupta, 2008), suggesting that different mantle isotopic end-members may be linked to distinct melting lithologies or to enrichments in volatiles and/or other metasomatic components (e.g., K_2O). In particular, oceanic island basalts (OIB) vary considerably in major element (Kogiso et al., 1997, 2003), trace element (Weaver, 1991), and isotopic composition (Zindler and Hart, 1986), consistent with derivation from diverse lithologies. While peridotite has long been thought to be the chief source lithology for basalt, partial melts of eclogite or pyroxenite may also contribute significantly during

* Corresponding author. Tel.: +1 612 625 0366; fax: +1 612 625 3819.
E-mail addresses: davis957@umn.edu (F.A. Davis), humayun@magnet.fsu.edu (M. Humayun), mmh@umn.edu (M.M. Hirschmann), coope359@umn.edu (R.S. Cooper).

0016-7037/$ - see front matter © 2012 Elsevier Ltd. All rights reserved.
http://dx.doi.org/10.1016/j.gca.2012.11.009

basalt petrogenesis (e.g., Hauri, 1996; Hirschmann and Stolper, 1996). Detection and quantification of contributions from recycled oceanic crustal lithologies in the source regions of OIB would provide key insights into the distribution of recycled lithologies in Earth's upper mantle as well as the processes that create, modify, and destroy heterogeneities in Earth's interior. Thus, it is of interest to develop geochemical techniques that can discriminate between different source lithologies of mantle-derived basalts.

Despite the reasonable first-order assumption that peridotite is a principle source of basalt in the upper mantle, the major element chemistry of OIB is inconsistent with partial melts of fertile peridotites formed at conditions similar to those likely present in the OIB source region (Takahashi et al., 1993). Specifically, most OIB have more FeO and less Al_2O_3 than near-solidus melts of garnet peridotite (Davis et al., 2011). Some factors that may account for these compositional differences include melting at greater depths where garnet stability is enhanced (Walter, 1998), enrichment of the peridotite source in volatiles (e.g., Hirose, 1997; Dasgupta et al., 2007), metasomatism by fluids (Pilet et al., 2005), or contributions from recycled lithologies (e.g., Chase, 1981; Hofmann and White, 1982; Weaver, 1991; Hauri, 1996; Kogiso et al., 1998, 2003). It is not yet possible to distinguish OIB as either products of enriched peridotite or recycled oceanic crust based solely on major element compositions, but trace elements may be useful additional petrogenetic indicators.

The elements Sc, Ti, V, Cr, Mn, Fe, Co, Ni, Cu, and Zn, collectively known as the first-row transition elements (FRTE), have emerged as potential indicators of basalt petrogenesis largely because they are compatible or only mildly incompatible during partial melting in Earth's mantle (e.g., Beattie et al., 1991; Humayun et al., 2004; Le Roux et al., 2011). This behavior leads to fractionations between pairs of FRTE that are distinct for different residual minerals, significantly affecting ratios of these elements in erupted lavas. Humayun et al. (2004) reported high-precision measurements of Fe/Mn in MORB, Hawaiian, and Icelandic basalts that revealed Hawaiian basalts have $Fe/Mn > 65$ and therefore form a population distinct from MORB and Icelandic basalts nearly all of which have $Fe/Mn < 62$. Further investigation showed that Fe/Mn ratios of lavas from Tahiti and, perhaps, St. Helena also are higher than those of MORB (Qin and Humayun, 2008). These studies concluded that the high Fe/Mn in OIB lavas was evidence of a deep mantle source, perhaps enriched in Fe through interaction with the core, but also considered the possibility that OIB could display such a signature if it were derived in some part from recycled oceanic crust.

The interpretation that lavas with high Fe/Mn derive in part from recycled oceanic crust was further developed by Sobolev et al. (2005, 2007). These studies showed that FRTE abundances and ratios (Ni, Cr, Fe/Mn, and Ni/Co) in olivine phenocrysts in many intraplate lavas form a population distinct from olivines in MORB (Sobolev et al., 2005, 2007), and that the characteristics of olivine phenocrysts from intraplate basalts were more similar to olivines experimentally equilibrated with pyroxenite-derived partial melts than those derived by partial melting of peridotite. Le Roux et al. (2010) surveyed Zn/Fe ratios of oceanic basalts and found that variations are greater in OIB than in MORB and that MORB Zn/Fe is nearly the same as that prevailing in the mantle as judged from peridotite xenoliths. Their measurements of Zn and Fe in cogenetic phenocryst suites suggested that Zn/Fe fractionation by olivine and opx cannot account for observed variations in OIB, and suggested that high Zn/Fe of many OIB require derivation from a cpx-rich source such as pyroxenite. They presented experimental determinations of partitioning of several divalent FRTE between basalt and olivine, opx, and cpx, confirming that residual cpx fractionates Zn/Fe and that olivine and opx do not (Le Roux et al., 2011). These experiments also contributed valuable partitioning measurements for other FRTE including Ni and Co.

There are few available data constraining the ability of garnet to fractionate FRTE, apart from a few measurements applicable to eclogite partial melting (Pertermann et al., 2004). Residual garnet exerts considerable influence on the partitioning of other trace elements, such as the heavy rare earth elements (Shimizu and Kushiro, 1975; Johnson, 1998), and has been inferred to have significant leverage over FRTE partitioning as well (Le Roux et al., 2011). It may be that some of the other FRTE (i.e., Sc, Ni, and Cu), as well as other compatible or modestly incompatible elements such as Ga and Ge, could be useful as petrogenetic indicators. It has been suggested, for example, that distinct Ga/Ge ratios of MORB and OIB are owing to differences in source lithology (Arevalo and McDonough, 2010b).

Here we present the results of FRTE partitioning experiments in the system peridotite + melt. The experiments were performed at 3 GPa near the solidus of fertile garnet lherzolite and using melt and mineral compositions previously determined to be in equilibrium during incipient partial melting (Davis et al., 2011). Several of these experiments produced liquids simultaneously saturated in olivine, opx, cpx, and garnet that are directly analogous to putative partial melts of peridotite in OIB source regions. The partition coefficients determined by these experiments form the basis for a melting model that we use to explore the hypothesis that FRTE ratios observed in natural OIB can result from peridotite partial melting.

2. METHODS

2.1. Experimental design

Starting materials were mixtures of reagent grade oxides and powdered glasses. Major and minor elements were added as SiO_2, TiO_2, Al_2O_3, Cr_2O_3, FeO, MnO, and MgO, and diopside, jadeite, and sanidine glasses. The mixtures were then homogenized with an agate mortar and pestle by grinding under ethanol for 1–2 h. Three different component mixtures were produced (Table 1): garnet lherzolite KLB-1ox.2, basalt 7, and a garnet powder with composition similar to those measured in Davis et al. (2011). KLB-1ox.2 was synthesized to approximate the composition of spinel lherzolite KLB-1 from Kilbourne Hole, New Mexico (Takahashi, 1986; Herzberg et al., 1990; Davis

Table 1
Major element compositions of starting materials.

	KLB-1ox.2	Basalt 7[a]	s.d.	MISEgrt
SiO_2	44.79	44.4	0.3	42.05
TiO_2	0.11	2.38	0.05	0.63
Al_2O_3	3.52	12.17	0.11	23.40
Cr_2O_3	0.32	0.11	0.02	1.06
FeO*	8.19	9.40	0.13	6.50
MnO	0.12	0.14	0.02	0.21
MgO	39.57	16.1	0.4	20.65
CaO	3.07	10.5	0.2	5.46
Na_2O	0.30	2.74	0.09	0.03
K_2O	0.01	1.06	0.05	0.00
Total	100.00	99.0		99.99
Mixtures	Perid:basalt:grt			
FRTE 1	20:80:0			
FRTE 1.1	30:70:0			
FRTE 2	20:70:10			
FRTE 2.1	20:70:10			

[a] Basalt 7 composition determined from EMP analysis of a glass fused at 1 GPa and 1600 °C in graphite. Peridotite and garnet compositions are weights of powders measured during weighing process.

et al., 2009), and basalt 7 mimics melt compositions determined by Davis et al. (2011) to be in equilibrium with a KLB-1 analog at its solidus (~1450 °C) at 3 GPa. These three components were combined in three different proportions (Table 1) and doped with 100 ppm each of Sc_2O_3, V_2O_5, CoO, NiO, Cu_2O, ZnO, Ga_2O_3, and GeO_2.

We emphasize that the chosen starting compositions are critical to the significance of the partitioning experiments we present. In their review of trace element partitioning, Blundy and Wood (2003) argued that tailoring partitioning experiments to specific magmatic processes was problematic because it is challenging to recreate conditions of near-solidus partial melting while preserving large crystals and melt pools for trace element analysis. We are able to overcome this obstacle by using melt and peridotite compositions previously determined to be in equilibrium near the peridotite solidus through iterative experiments (Davis et al., 2011). This technique produces large pools of melt, saturated in all four mantle mineral phases with compositions that are similar to those present during incipient partial melting of natural garnet peridotite.

Starting powders were packed into graphite crucibles with an inner diameter of ~1 mm and placed in Pt capsules with outer diameter ~3.8 mm. A ~500 μm long piece of Pt wire (~50 μm diameter) was added to two capsules to be used as a monitor of experimental f_{O2}. Additional graphite powder was packed into the capsules, which were then coned shut and kept overnight at 110 °C in a vacuum oven. The capsules were then welded shut and the cones flattened. The capsules were housed in crushable MgO spacers, inserted first into a graphite furnace, then into a $BaCO_3$ pressure cell, and wrapped in a thin piece of Pb foil.

Experiments were performed in a ½″ piston cylinder apparatus at 3 GPa (±0.1 GPa, Xirouchakis et al., 2001). Experiments were first heated above the intended dwell temperature to produce an initially large melt fraction from which to crystallize a few large minerals for laser ablation inductively-coupled plasma mass spectrometry (LA-ICP-MS). The temperature was held at this initial temperature (T_1) for two hours before cooling at 0.1 or 0.3 °C/min to the dwell temperature (T_2) and held for 24–84 h, as detailed in Table 2.

The experimental runs were quenched by opening the sample load pressure valve slightly, thereby inducing rapid sample decompression, and then immediately cutting power to the furnace, a method similar to that described by Putirka et al. (1996). This inhibits the formation of quench crystals in the melt pools and increases the likelihood of recovering glassy regions. Capsules were sectioned vertically and each half was mounted in epoxy on a brass plug.

Table 2
Experimental details.

run	T_1 (°C)	T_2 (°C)	Cooling rate (°C/min)	Dwell (h)	logf_{o2}[a]	Starting mix	Phases[b]	Pt wire[c]: Pt (wt.%)	s.d.	Fe (wt.%)	s.d.
A779	1565	1465	0.1	24		FRTE 1.0	glass + cpx + ol				
A781	1560	1460	0.1	24		FRTE 1.0	glass + cpx + ol				
A784	1565	1465	0.1	24		FRTE 1.1	glass + cpx + ol + opx + grt				
A786	1565	1465	0.1	24		FRTE 1.1	glass + cpx + ol + opx				
A788	1565	1465	0.3	84		FRTE 1.1	glass + cpx + ol + opx				
A791	1650	1465	0.1	48		FRTE 1.1	glass + cpx + ol + opx				
A799	1650	1475	0.1	48		FRTE 1.1	glass + cpx + ol + opx				
A806	1650	1465	0.1	48		FRTE 2.0	glass + cpx + ol + opx + spl				
A825	1520	1470	0.1	48		FRTE 2.0	glass + cpx + ol + opx + grt				
A830	1520	1470	0.1	48		FRTE 2.0	glass + cpx + ol + opx				
A834	1520	1470	0.1	48		FRTE 2.1	qnch + cpx + ol + grt				
A842	1520	1470	0.1	48	−6.4	FRTE 2.1	glass + cpx + ol + opx	86.9	0.6	13.29	0.14
A847	1520	1470	0.1	48	−5.9	FRTE 2.1	qnch + cpx + ol + grt	88.3	0.6	11.8	0.2

[a] From Fe content of Pt wire and coexisting melt (Medard et al., 2008).
[b] glass indicates that an experiment contained glassy and quench-crystallized regions in its melt pool, qnch indicates no glass, ol = olivine, grt = garnet, spl = Mg–Al spinel.
[c] $n = 8$ for both A842 and A847.

Samples were polished using dry diamond powder on nylon pads to a finish of 0.25 μm and then coated with a thin (5–20 nm) conductive carbon layer.

2.2. Analytical techniques

2.2.1. Electron microprobe (EMP)

Mineral and melt phases were identified using back-scattered electron (BSE) images and energy dispersive spectra (EDS), collected with the JEOL JXA-8900 electron microprobe at the University of Minnesota. Wavelength dispersive spectrometry (WDS) maps were collected for some samples to reveal the presence of compositional zoning in minerals.

Major element compositions of minerals were determined by WDS analysis by collecting at least 20 individual analytical spots from each mineral phase present in the capsule. In cpx grains with compositional gradients, an effort was made to target both low-Al and high-Al regions of the crystals. Mineral analysis was performed with a focused spot (<1 μm), an accelerating voltage of 15 kV, and a beam current of 15 nA. Count times were 20 s on-peak and 10 s off-peak for all oxides except Na_2O. Count times for Na_2O were 10 s on-peak and 5 s off-peak and Na_2O was measured on the first pass of the spectrometer to reduce migration under the beam. Individual analytical points were excluded from the average if totals were $\geqslant$101% or <99%, or if the analyses gave poor stoichiometry (±0.01 total cations) calculated on a 4- (olivine, spinel), 6- (pyroxenes), or 12- (garnet) oxygen basis.

Melt analyses were performed with a 10 μm beam and current of 10 nA. Glassy regions of the melt pool were analyzed when available, otherwise heterogeneous quenched melt pools were analyzed at least 50 μm away from the nearest equilibrium crystals. When analyzing glass, at least 17 analytical points were collected and averaged. When analyzing heterogeneous quench products, analytical points were selected by placing between 82 and 179 spots along one or several lines, sampling at regularly spaced intervals of 15 μm. This random selection of analytical points reduces the possibility of collecting a compositionally biased dataset, as can result from manual spot selection. The number of analytical points collected from the quench products was sufficient to give errors of the mean ($\sigma/\sqrt{n}$, 68% confidence interval) that were within 1% relative of the average concentrations for all major elements and TiO_2, and within better than 10% of other minor elements. Measurements of both glassy and crystalline quench regions of A825 and A830 provide a further check on the accuracy of melt compositions determined from heterogeneous quench products; these results are presented in Section 3.2.2.

Pt f_{O2} sensors loaded into two of the experiments (A842 and A847) were analyzed with a 5 μm spot and 15 nA beam current. Pt and Fe metal standards were used. Fe and Pt contents were measured by counting on the K_α and M_α peaks, respectively. Points were collected across the exposed area of the metal, but did not reveal any compositional zonation. Compositions presented in Table 2 are averages of all analyses that returned totals between 99% and 101%.

2.2.2. Laser ablation inductively-coupled plasma mass spectrometry (LA-ICP-MS)

Major and trace elements were analyzed by LA-ICP-MS using a New Wave UP193FX (193 nm) ArF excimer laser ablation system coupled to a Thermo Element XR sector-field ICP-MS at the Plasma Analytical Facility, Florida State University. Major element analysis followed Humayun et al. (2010). Spot analyses were performed with 25 μm or 50 μm beam diameters, 10 s dwell times; line scans and rasters were performed with 25 μm (5 μm/s) or 50 μm (10 μm/s) beam diameters with scan speeds given in parentheses. Counting on the Element XR was initiated before firing the laser and continued after the laser was turned off to collect ample gas blanks. The resulting blank intensities were subtracted from the peak intensities. These corrected intensities were then converted to oxide (for major elements) or element concentrations by comparison to a relative sensitivity factor (RSF, Humayun et al., 2007; Gaboardi and Humayun, 2009):

$$\mathrm{RSF} = \frac{C_i/C_a}{I_i/I_a}$$

where C_i is the concentration of the oxide or element of interest, I_i is the peak intensity of the isotope being monitored, C_a is the concentration of SiO_2 or MgO, and I_a is the peak intensity of ^{29}Si or ^{25}Mg; SiO_2 was used to calculate RSF in an early session, and MgO in all subsequent sessions. RSFs were determined by averaging triplicate analyses of USGS reference glasses BHVO2 (Wilson, 1997b), BCR2 (Wilson, 1997a), BIR1 (Govindaraju, 1994), and GSE1. Other standards run as controls included the NIST SRM 610 (Jochum et al., 2011) and the MPI-DING glasses, KL2-G, ML3B-G, GOR132-G and T1-G (Jochum et al., 2006). Reference glass GSE1 was tested before and after each session to check if the RSF value had shifted during the session. During two sessions, the Si RSF was found to have shifted. In the first instance, the Si RSF used for sample A791, run in the middle of the session, was adjusted along the line defined by the morning and afternoon RSF determinations to give SiO_2 in agreement with microprobe measurements of A791 olivine. In subsequent sessions, glass standards were reanalyzed multiple times throughout the day to allow for adjustments in RSFs if necessary.

Linear traverses were filtered by plotting concentration against distance for important indicator elements and the portions of the data that corresponded to a single phase were averaged to obtain the phase compositions. For example, if a scan began in a cpx grain and passed into a melt region, the portion of the analysis where cpx was sampled and the portion where melt was sampled were identified by incompatible elements like TiO_2 and K_2O.

Some post-collection filtering was applied to find average compositions of minerals and melts. To avoid analytical spots that might have sampled more than one phase, individual mineral spots were excluded from averaging using several criteria. Olivine analyses were excluded if calculated K_D^{Mg-Fe} was found to fall outside the range expected for olivines and melts in equilibrium (Toplis, 2005), or if incompatible elements were found in excessive concentrations

(e.g., $Al_2O_3 > 0.5$ wt.%). Other phases were excluded from averaging if their calculated stoichiometries fell outside an acceptable range (±0.05 cations), similar to treatment of EMP analyses (Section 2.2.1) but with a somewhat more permissive filter. Pyroxenes and garnets from experiments A786, A825, and A842 all gave calculated stoichiometries that fell outside this range, and measurements of some major elements in these phases differed by >10% relative from measurements by EMP. This may have been due to drifting RSF values, which we discuss in greater detail in Section 3.2.

3. RESULTS

3.1. Phase relations and experimental textures

The final melt composition from the iterative experiments of Davis et al. (2011) was chosen as the starting melt composition of this study to ease the process of producing experiments with basaltic melt in equilibrium with a fertile lherzolite assemblage of olivine, orthopyroxene, clinopyroxene, and garnet. Additionally, these minerals and melts should have major element compositions representative of residues and melts plausibly found in the OIB source region. The resulting mineral assemblage in some experiments achieved multiple saturation in all four mineral phases (Fig. 1), but the added complexity of ramping above the temperature of interest and then cooling resulted in several phase assemblages that were different from the intended olivine + opx + cpx + garnet + melt (Table 2).

A crystallization sequence can be inferred from the presence or absence of phases in experiments and from their textures. In experiments that had a difference between T_1 and $T_2 > 50$ °C, commonly one large olivine crystal was found in the center of a single large cpx crystal, while in experiments with $T_1 - T_2 = 50$ °C several small olivine grains were present at the bottom of the capsule. This suggests that olivine is the liquidus phase. The order of opx and cpx crystallization is less certain. Typically, opx was surrounded by a single large cpx grain, which suggests that opx crystallization occurred prior to or concurrent with cpx crystallization. Garnet crystallized in five experiments, and in one experiment spinel formed as the aluminous phase instead of garnet. When garnet or spinel were present they were in contact with the melt and, in all but one experiment, were found surrounded entirely by melt (in the plane of view). This suggests that garnet or spinel was the last crystallizing phase.

Several experiments failed to crystallize garnet, possibly because of its low proportion in the mineral mode of the peridotite and its position at the end of the crystallization sequence. In the single experiment in which spinel was produced, we believe it formed during the cooling step, owing to the stabilization of spinel at high temperature at 3 GPa (Robinson and Wood, 1998), and did not back-react to garnet during the remainder of the cooling and dwell steps. This result was fortuitous as it allowed us to measure spinel-melt partitioning. The retardation of saturation in highly aluminous phases produced in some cases cpx grains with high-Al zones, which presumably grew during a phase of crystallization when the coexisting melt was supersaturated in garnet. This presented a challenge for determining cpx partition coefficients (see Section 3.2.1).

In all experiments, at least some portion of the melt crystallized during quench, but glassy regions were preserved in most samples. In experiments that contained both glass and quench-crystallized melt, the glassy regions were usually located away from crystals or the walls of the capsule (Fig. 1). In one exceptional experiment, A786, pressure was dropped much more rapidly than in the others during quench. This experiment exhibited glassy regions in contact with the crystals and capsule walls, and was the only experiment that had melt present at the bottom of the capsule (Fig. 1). These observations suggest that in this experiment significant remelting of the residue occurred during the quench step. This experiment serves as qualitative evidence that glass formation is promoted by the so-called "pressure quench" method originally described by Putirka et al. (1996), widely used in piston cylinder laboratories (e.g., Balta et al., 2011; Krawczynski and Grove, 2012), and that the magnitude of the pressure drop affects the extent of remelting that can occur.

Ni and Cu were not detected or were in extremely low concentrations in minerals and melts of all experiments. It has been previously observed that Ni is not contained by Pt-graphite capsules (Matzen et al., 2009), and Fellows and Canil (2012) observed severe Cu-loss from piston cylinder experiments run in Pt and Pt-graphite capsules. They were able to reduce Cu-loss by encapsulating their samples in Re-foil. It is interesting to note that Fellows and Canil (2012) observed more rapid loss of Cu from experiments lined with graphite than from those in direct contact with Pt, which suggests that graphite plays a role in mobilizing Ni and Cu. Le Roux et al. (2011) present measurements of Ni concentrations in experiments run in graphite capsules, but their experiments were doped at a higher concentration (1 wt.%) than in our experiments.

3.2. Compositions and partition coefficients of experimental products

Average major and trace element compositions of mineral and melt phases are presented in Tables 3–12. Most measurements of major element compositions of melts, olivine, opx, garnet, and spinel by EMP and LA-ICP-MS agree to within 10% relative. Agreement between the two methods is not as good for some minor elements (e.g., Cr_2O_3, MnO, CaO in olivine). Likely sources of disagreement include imprecise measurements of minor elements like Mn and Cr by EMP and shifts in RSF values during LA-ICP-MS sessions. Si RSF shifts were observed during two sessions (A788, A791, A806, A842, and A847 were analyzed in these sessions).

While perturbations to the RSFs can affect the absolute concentrations reported from LA-ICP-MS measurements, the RSF is cancelled out in the calculation of partition coefficients. Thus, partition coefficients derived from LA-ICP-MS analysis are accurate even when absolute concentrations disagree with those measured by EMP. To better demonstrate this, we compare partition coefficients derived by the

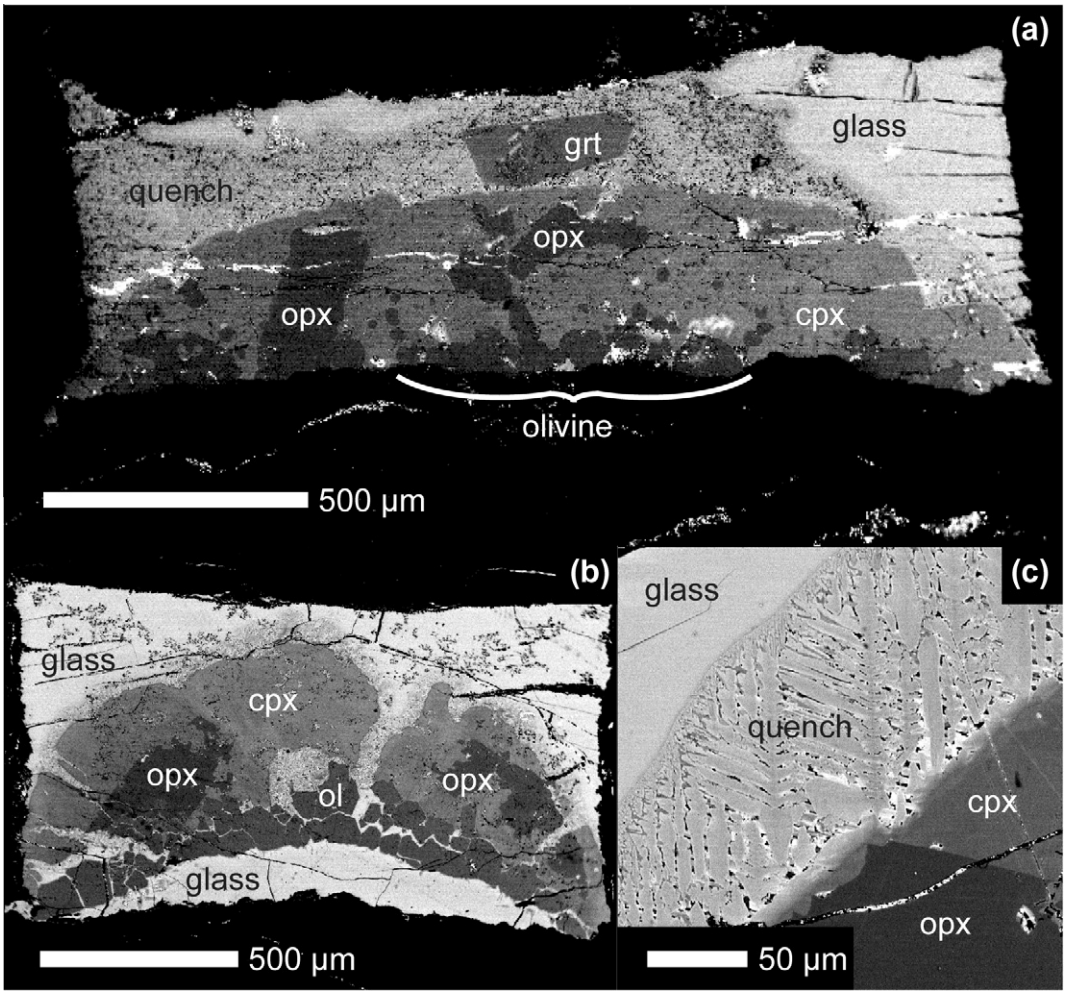

Fig. 1. Back-scattered electron (BSE) images of experimental textures. (a) Section from experiment A825 showing the textures of the mineral and melt phases. Small olivines were commonly located at the bottom of capsules with a large, single cpx crystal partially enveloping opx crystals. All garnets were found to be in contact with melt. (b) Experiment A786 demonstrates glass formation during pressure-quenching (Putirka et al., 1996). This experiment was quenched with a much larger drop in pressure than other experiments, and the melt present at the bottom of the capsule suggests extensive remelting during quench. (c) Close-up of glassy and quench-crystallized melt textures from experiment A799. Dendritic quench crystals nucleate on equilibrium crystals and on the edges of the graphite capsule.

two methods. Mineral/melt partition coefficients for those FRTE that were measured by EMP are included in Tables 4, 6 and 7 (cpx/melt partition coefficients were not calculated from EMP data because of chemical zonation in cpx described in Section 3.2.1). For all olivine–melt pairs that exhibit equilibrium K_D^{Mg-Fe}, D_{Fe} and D_{Mn} agree within error. All but three measurements of $D_{Fe}^{opx/melt}$ and three out of four $D_{Fe}^{grt/melt}$ measurements agree within error. Average partition coefficients calculated from all experiments using each analytical method are in remarkably close agreement: $D_{Fe}^{ol/melt} = 1.03 \pm 0.02$ (LA-ICP-MS) and 1.01 ± 0.01 (EMP), $D_{Mn}^{ol/melt} = 0.78 \pm 0.01$ (LA-ICP-MS) and 0.78 ± 0.07 (EMP), $D_{Fe}^{opx/melt} = 0.546 \pm 0.010$ (LA-ICP-MS) and 0.528 ± 0.008 (EMP), $D_{Mn}^{opx/melt} = 0.64 \pm 0.01$ (LA-ICP-MS) and 0.69 ± 0.06 (EMP), $D_{Fe}^{grt/melt} = 0.654 \pm 0.007$ (LA-ICP-MS) and 0.677 ± 0.003 (EMP), $D_{Mn}^{grt/melt} = 1.24 \pm 0.02$ (LA-ICP-MS) and 1.26 ± 0.05 (EMP). LA-ICP-MS partition coefficients (Table 13) are used in partial melting models presented in Section 4 as they are generally more precise than those determined by EMP.

3.2.1. Compositional zoning in cpx

Rims of some cpx show an extreme enrichment in Al_2O_3 compared with equilibrium cpx compositions from iterative sandwich experiments performed in the same system (Davis et al., 2011). For example, cpx in A781 has 5.7 wt.% Al_2O_3 in its core, less than the equilibrium cpx Al_2O_3 concentration of 6.1 wt.% measured by Davis et al. (2011), but the concentration of Al_2O_3 increases dramatically in the outer 100 μm of the crystal to >9 wt.% (Fig. 2). Concentrations of the FRTE in cpx are correlated with Al_2O_3 (Fig. 2), so determination of cpx/melt partition coefficients for a given experiment depends on what is interpreted to be the equilibrium cpx composition. Elevated Al_2O_3 concentrations in cpx rims may be related to a high activity of Al_2O_3 in the absence of garnet, which was not present in many of the

Table 3
Electron microprobe measurements of major elements in experimental melt.

	A779	s.d.	A781	s.d.	A784	s.d.	A786	s.d.	A788	s.d.	A791	s.d.	A799	s.d.	A806	s.d.
n	20		32		20		20		20		20		20		20	
Phase	Glass		Glass		Glass		Glass		Glass		Glass		Glass		Glass	
SiO_2	44.1	0.3	42.6	0.3	42.4	0.2	43.0	0.3	43.0	0.3	42.34	0.16	42.74	0.19	41.55	0.15
TiO_2	2.86	0.06	3.28	0.08	3.45	0.08	2.92	0.05	3.35	0.07	2.89	0.06	2.66	0.06	3.24	0.05
Al_2O_3	13.42	0.13	14.95	0.13	12.36	0.15	14.0	0.2	14.99	0.13	13.13	0.08	12.74	0.10	14.40	0.10
Cr_2O_3	0.06	0.02	0.03	0.03	0.03	0.02	0.06	0.02	0.04	0.02	0.03	0.02	0.05	0.03	0.03	0.03
FeO^*	9.08	0.12	9.92	0.14	8.23	0.10	8.94	0.13	9.96	0.11	8.13	0.12	9.17	0.13	8.61	0.09
MnO	0.13	0.03	0.14	0.02	0.13	0.03	0.12	0.03	0.13	0.02	0.14	0.03	0.15	0.03	0.15	0.03
MgO	15.68	0.13	14.73	0.18	16.01	0.15	15.5	0.3	14.60	0.17	15.56	0.13	15.23	0.14	14.00	0.13
CaO	9.20	0.13	8.55	0.12	9.33	0.09	9.45	0.14	8.77	0.14	9.84	0.11	9.59	0.09	9.48	0.09
Na_2O	2.67	0.07	2.91	0.10	3.48	0.11	2.80	0.11	3.05	0.08	2.98	0.07	2.84	0.08	3.16	0.09
K_2O	1.39	0.06	1.75	0.06	1.72	0.05	1.40	0.04	1.64	0.05	1.37	0.04	1.28	0.04	1.75	0.05
Total	98.6		98.9		97.2		98.2		99.5		96.41		96.44		96.37	

	A825	s.d.	A825	err	A830	s.d.	A830	err	A834	err	A842	err	A847	err
n	20		124		17		82		111		167		104	
Phase	Glass		Quench		Glass		Quench		Quench		Quench		Quench	
SiO_2	43.54	0.11	42.9	0.2	44.6	0.2	44.43	0.16	44.67	0.18	43.26	0.06	42.9	0.3
TiO_2	3.03	0.05	3.028	0.018	2.50	0.08	2.467	0.011	2.867	0.014	2.538	0.008	3.24	0.03
Al_2O_3	13.44	0.11	13.20	0.05	14.61	0.13	14.51	0.03	12.54	0.05	14.76	0.02	11.76	0.06
Cr_2O_3	0.04	0.04	0.033	0.003	0.114	0.019	0.100	0.003	0.050	0.003	0.118	0.003	0.030	0.003
FeO^*	7.86	0.10	7.88	0.04	7.89	0.11	7.96	0.03	9.92	0.08	10.16	0.02	10.69	0.11
MnO	0.16	0.03	0.137	0.003	0.13	0.03	0.142	0.003	0.141	0.003	0.144	0.003	0.144	0.004
MgO	14.92	0.12	14.53	0.11	15.60	0.17	15.51	0.07	15.26	0.11	14.52	0.07	14.3	0.2
CaO	9.43	0.09	9.36	0.07	9.93	0.13	9.84	0.06	9.02	0.10	8.88	0.03	8.93	0.11
Na_2O	3.05	0.08	2.62	0.06	2.65	0.10	2.52	0.05	2.53	0.04	2.14	0.03	2.87	0.12
K_2O	1.39	0.04	1.24	0.08	1.23	0.04	1.20	0.04	1.39	0.06	1.108	0.013	1.67	0.11
Total	96.86		94.9		99.3		98.67		98.38		97.62		96.6	

Table 4
Electron microprobe measurements of major elements in experimental olivine.

	A779	s.d.	A781	s.d.	A784	s.d.	A786	s.d.	A788	s.d.	A791	s.d.	A799	s.d.
n	20		20		17		19		19		12		20	
SiO_2	41.0	0.3	40.8	0.3	40.95	0.16	40.20	0.15	40.53	0.15	41.42	0.25	41.14	0.17
TiO_2	0.01	0.02	0.02	0.02	0.02	0.02	0.02	0.02	0.01	0.02	0.02	0.01	0.022	0.014
Al_2O_3	0.153	0.016	0.17	0.02	0.14	0.01	0.16	0.02	0.16	0.02	0.15	0.02	0.145	0.008
Cr_2O_3	0.05	0.03	0.03	0.02	0.03	0.03	0.05	0.02	0.03	0.02	0.06	0.03	0.06	0.02
FeO*	8.3	0.3	10.16	0.30	8.66	0.17	9.23	0.14	10.58	0.18	6.71	0.90	8.29	0.33
MnO	0.09	0.02	0.11	0.02	0.11	0.02	0.10	0.02	0.12	0.02	0.09	0.03	0.093	0.010
MgO	49.46	0.43	48.76	0.24	49.92	0.20	49.05	0.18	48.57	0.23	52.08	0.81	50.37	0.32
CaO	0.246	0.019	0.23	0.02	0.23	0.02	0.23	0.02	0.22	0.02	0.22	0.02	0.23	0.02
Na_2O	0.026	0.016	0.04	0.02	0.03	0.02	0.04	0.02	0.03	0.02	0.02	0.02	0.038	0.018
K_2O	0.000	0.010	0.004	0.014	0.005	0.011	0.011	0.011	0.006	0.012	-0.001	0.012	0.003	0.011
Total	99.4		100.3		100.10		99.10		100.26		100.77		100.39	
K_D^{Fe-Mg}	0.29		0.31		0.34		0.33		0.32		0.25		0.27	
D_{Ti}	0.004	0.007	0.005	0.005	0.007	0.005	0.006	0.006	0.003	0.005	0.006	0.005	0.008	0.005
D_{Cr}	0.9	0.6	0.8	1.0	0.8	0.9	0.9	0.5	0.6	0.6	1.8	1.5	1.2	0.8
D_{Mn}	0.7	0.2	0.8	0.2	0.8	0.2	0.8	0.3	0.9	0.2	0.6	0.2	0.62	0.15
D_{Fe}	0.91	0.04	1.01	0.03	1.02	0.02	1.02	0.02	1.05	0.02	0.8	0.4	0.90	0.04

	A806	s.d.	A825	s.d.	A830	s.d.	A834	s.d.	A842	s.d.	A847	s.d.
n	19		4		6		20		18		20	
SiO_2	41.26	0.17	41.33	0.15	41.06	0.10	40.7	0.6	41.06	0.18	40.78	0.19
TiO_2	0.008	0.016	0.02	0.02	0.031	0.016	0.032	0.019	0.011	0.016	0.024	0.018
Al_2O_3	0.169	0.012	0.175	0.016	0.18	0.02	0.173	0.016	0.17	0.02	0.187	0.013
Cr_2O_3	0.09	0.03	0.04	0.02	0.07	0.03	0.03	0.02	0.08	0.03	0.043	0.016
FeO*	6.5	0.2	8.29	0.11	8.34	0.09	9.98	0.15	9.8	0.2	10.50	0.16
MnO	0.10	0.02	0.10	0.03	0.11	0.02	0.10	0.02	0.11	0.02	0.11	0.02
MgO	51.11	0.27	50.53	0.08	50.82	0.10	48.5	0.6	48.9	0.2	48.04	0.19
CaO	0.22	0.02	0.237	0.014	0.23	0.02	0.257	0.018	0.27	0.03	0.248	0.019
Na_2O	0.028	0.019	0.022	0.014	0.030	0.017	0.08	0.07	0.04	0.02	0.042	0.016
K_2O	0.004	0.012	-0.002	0.01	0.001	0.016	0.018	0.018	0.004	0.012	0.003	0.011
Total	99.5		100.74		100.88		99.9		100.5		99.98	
K_D^{Fe-Mg}	0.21		0.31		0.32		0.32		0.29		0.30	
D_{Ti}	0.008	0.005	0.002	0.005	0.007	0.007	0.012	0.006	0.011	0.007	0.005	0.007
D_{Cr}	1.1	0.7	2.7	2.8	1.0	0.9	0.6	0.3	0.7	0.4	0.7	0.2
D_{Mn}	0.60	0.14	0.62	0.18	0.8	0.2	0.8	0.2	0.70	0.17	0.80	0.17
D_{Fe}	0.87	0.04	0.73	0.02	1.02	0.02	1.04	0.02	0.99	0.02	0.99	0.02

experiments. In these experiments, the first cpx to crystallize may have had lower Al_2O_3 than the equilibrium composition and then partially reequilibrated with the high Al_2O_3 melt (15 wt.%) by diffusion during the dwell step. It is also possible that the increased activity of Al_2O_3 led to an increase in Al_2O_3 in the late-forming cpx, so that the rim represents a crystal growth profile.

Irrespective of the cause of zonation, the rim cpx has more Al_2O_3, and if used to calculate cpx/melt partition coefficient, gives $D_{Al}^{cpx/melt} = 0.66$, which is much higher than the $D_{Al}^{cpx/melt} = 0.48$ expected for equilibrium cpx (Davis et al., 2011). Because we are interested in the cpx/melt partition coefficients relevant to peridotite partial melting, we used the known equilibrium $D_{Al}^{cpx/melt}$ from Davis et al. (2011) to determine $D^{cpx/melt}$ for the FRTE. Measured concentrations of the FRTE vary nearly linearly with Al_2O_3 content in the cpx crystals (Fig. 2), so we determine the equilibrium concentrations of FRTE by linear regression to the Al_2O_3 concentration that gives the known equilibrium value of $D_{Al}^{cpx/melt} = 0.48$ (Fig. 2). This is not an ideal method to determine equilibrium partition coefficients, but zoned cpx may be an unavoidable by-product of growing large minerals for trace element analysis (e.g., Hart and Dunn, 1993). Close agreement of our cpx partition coefficients with trends in other experimental datasets (Section 4.1) suggests that this is a reasonable method for estimating equilibrium partitioning of FRTE in zoned cpx.

3.2.2. Compositions of glassy and quench crystallized melt phases

To test whether our EMP measurements of heterogeneous quenched melt products accurately determine the composition of the melt phase, we analyzed both glassy and quench-crystallized portions of melt pools in two of the experiments in which both were present (A825 and A830, Table 3). Measurements from A830 are the same within error for all elements. For A825, the measurement from the quench-crystallized region is slightly lower in SiO_2 and Al_2O_3 (<1% relative) and is 14% lower in Na_2O than the measurement of glass. We also measured glassy and crystalline regions in four experiments by LA-ICP-MS laser traverses and found the average composition was the same in each for all elements, except Na_2O, which is lower when measured in the quench-crystallized region,

Table 5
Electron microprobe measurements of major elements in experimental orthopyroxene.

	A784	s.d.	A786	s.d.	A788	s.d.	A791	s.d.	A799	s.d.
n	19		10		9		15		13	
SiO_2	55.7	0.2	54.81	0.14	52.9	0.9	56.2	0.2	55.3	0.3
TiO_2	0.160	0.019	0.164	0.019	0.32	0.05	0.17	0.03	0.20	0.02
Al_2O_3	4.49	0.16	4.64	0.15	8.6	1.6	4.77	0.18	4.8	0.4
Cr_2O_3	0.34	0.02	0.36	0.03	0.24	0.04	0.35	0.02	0.35	0.03
FeO*	4.14	0.06	4.53	0.08	6.2	0.3	3.95	0.09	4.62	0.10
MnO	0.09	0.03	0.100	0.017	0.11	0.02	0.09	0.02	0.09	0.02
MgO	32.9	0.2	32.20	0.15	29.9	0.7	33.62	0.16	32.3	0.3
CaO	2.21	0.08	2.45	0.10	2.2	0.3	2.09	0.06	2.64	0.18
Na_2O	0.24	0.04	0.25	0.02	0.34	0.03	0.230	0.018	0.281	0.018
K_2O	−0.003	0.008	0.003	0.007	0.011	0.013	0.001	0.012	0.009	0.016
Total	100.3		99.50		100.8		101.5		100.6	
D_{Ti}	0.045	0.005	0.055	0.007	0.094	0.015	0.057	0.009	0.070	0.009
D_{Cr}	11	7	6	3	5	3	10	7	7	3
D_{Mn}	0.6	0.2	0.8	0.2	0.8	0.2	0.7	0.2	0.59	0.19
D_{Fe}	0.488	0.009	0.500	0.012	0.62	0.03	0.461	0.013	0.482	0.013

	A806	s.d.	A825	s.d.	A830	s.d.	A842	s.d.
n	18		19		11		8	
SiO_2	53.9	0.4	53.9	0.7	53.9	0.5	53.8	0.9
TiO_2	0.19	0.03	0.22	0.04	0.219	0.016	0.29	0.03
Al_2O_3	6.8	0.5	6.9	1.2	7.0	0.7	6.9	1.3
Cr_2O_3	0.49	0.05	0.43	0.12	0.52	0.09	0.39	0.06
FeO*	3.97	0.15	4.9	0.2	4.98	0.16	5.1	0.4
MnO	0.087	0.013	0.10	0.02	0.100	0.016	0.10	0.01
MgO	31.8	0.3	31.4	0.5	31.3	0.4	31.4	0.8
CaO	2.26	0.11	2.23	0.12	2.34	0.08	2.33	0.12
Na_2O	0.25	0.03	0.27	0.03	0.27	0.03	0.25	0.03
K_2O	0.005	0.015	0.004	0.013	−0.002	0.010	−0.003	0.011
Total	99.8		100.5		100.6		100.5	
D_{Ti}	0.058	0.008	0.072	0.013	0.086	0.007	0.107	0.014
D_{Cr}	15	15	11	8	4.5	1.1	3.4	0.4
D_{Mn}	0.56	0.13	0.75	0.20	0.74	0.19	0.73	0.12
D_{Fe}	0.445	0.018	0.61	0.03	0.62	0.02	0.53	0.04

although there is more scatter in intensity measurements of all elements from the crystallized region than in the glass (see Appendix for details).

Mineral/melt partition coefficients of FRTE for each experiment were determined by dividing the average mineral compositions (calculated compositions for zoned cpx) by average melt compositions (Fig. 3). The partition coefficients presented in Table 13 are averages of the individual experimental partition coefficients as determined by LA-ICP-MS (Tables 9–12). In two experiments (A791 and A806), no LA-ICP-MS measurements of olivine gave equilibrium values for K_D^{Mg-Fe} (Section 2.2.2), so olivine/melt partition coefficients from these experiments were not included in the average.

3.2.3. Pt–Fe alloy and experimental f_{O2}

Measurement of the Fe concentration in pieces of Pt wire added to two capsules allows us to determine the f_{O2} of these experiments (Table 2). Following the method of Medard et al. (2008), we use the exchange of Fe between Pt metal and coexisting melt to determine f_{O2} in the system. As observed by Medard et al. (2008), f_{O2} is not held constant by the Pt-graphite capsule assemblage, but varies slightly below the carbon–CO (CCO) buffer. Logf_{O2} for the two experiments varied between −6.4 and −5.9 (CCO-0.7 to CCO-0.2, Frost and Wood, 1997). From these calculations we can estimate the fraction of Fe^{3+} in the melt phases of our experiments. $Fe^{3+}/\Sigma Fe$ in the melts of A842 and A847 were calculated to be 0.04 and 0.05, respectively (Kress and Carmichael, 1991). If we treat Fe^{3+} as perfectly incompatible (an exaggeration), then mineral/melt partition coefficients for Fe^{2+} would be 4–6% higher than ΣFe partition coefficients. Estimated error of individual Fe mineral/melt partition coefficients varies between 1% and 11% relative (mean = 5%). It is likely that differences between D_{Fe2+} and D_{Fe} are within the error of our measurements.

4. DISCUSSION

4.1. Derivation of bulk residue/melt exchange coefficients from mineral/melt D

A key observation of the behavior of FRTE during melting in the mantle is that mineral/mineral and mineral/melt exchange coefficients remain nearly constant over a range of pressures and temperatures. This has been observed previously in natural phenocryst pairs (Le Roux et al., 2010) and experimental minerals and melts (Le Roux

Table 6
Average electron microprobe measurements of major elements in experimental clinopyroxene.[a]

	A779	s.d.	A781	s.d.	A784	s.d.	A786	s.d.	A788	s.d.	A791	s.d.	A799	s.d.
n	19		16		19		10		15		17		19	
SiO_2	53.9	0.5	52.9	1.4	53.5	0.8	52.8	0.7	52.8	0.9	53.4	0.8	53.5	0.7
TiO_2	0.30	0.04	0.38	0.14	0.34	0.09	0.33	0.06	0.42	0.09	0.39	0.07	0.32	0.07
Al_2O_3	6.2	0.6	8	2	7.2	1.3	6.9	1.0	7.9	1.4	7.9	1.1	6.7	1.0
Cr_2O_3	0.34	0.04	0.27	0.06	0.35	0.07	0.39	0.05	0.35	0.05	0.33	0.05	0.36	0.06
FeO*	4.57	0.14	4.7	0.3	4.12	0.14	4.53	0.16	5.1	0.3	4.00	0.12	4.58	0.12
MnO	0.11	0.03	0.105	0.019	0.104	0.018	0.09	0.03	0.108	0.017	0.11	0.02	0.102	0.017
MgO	24.1	1.0	22	3	23.5	1.5	22.8	1.4	22.2	1.7	22.4	1.2	23.4	1.3
CaO	9.6	0.8	11	2	10.1	0.8	10.4	1.1	10.6	1.2	11.3	0.7	10.2	0.9
Na_2O	0.91	0.09	1.2	0.3	1.06	0.15	1.01	0.09	1.14	0.17	1.09	0.10	1.02	0.13
K_2O	0.005	0.008	0.005	0.013	0.002	0.010	0.007	0.014	0.012	0.014	0.010	0.011	0.015	0.015
Total	100.0		99.9		100.3		99.3		100.6		100.9		100.1	

	A806	s.d.	A825	s.d.	A830	s.d.	A834	s.d.	A842	s.d.	A847	s.d.
n	18		7		36		19		9		6	
SiO_2	51.6	0.6	52.3	0.4	52.9	0.4	53.2	0.3	52.6	0.3	53.3	0.3
TiO_2	0.44	0.08	0.41	0.05	0.33	0.04	0.38	0.06	0.36	0.03	0.44	0.03
Al_2O_3	10.1	1.1	9.4	0.7	7.9	0.5	7.3	0.4	8.7	0.3	7.5	0.4
Cr_2O_3	0.37	0.11	0.47	0.04	0.60	0.07	0.36	0.04	0.55	0.05	0.20	0.03
FeO*	3.9	0.2	4.35	0.13	4.35	0.10	4.67	0.18	4.82	0.17	4.8	0.3
MnO	0.120	0.019	0.13	0.04	0.12	0.02	0.12	0.03	0.106	0.018	0.097	0.011
MgO	21.0	0.9	21.7	0.6	22.8	0.5	21.5	0.9	21.8	0.6	20.7	0.6
CaO	11.5	0.4	10.9	0.5	10.7	0.4	11.7	0.9	10.8	0.7	12.0	0.8
Na_2O	1.17	0.11	1.07	0.05	0.95	0.07	1.19	0.10	1.07	0.06	1.34	0.04
K_2O	0.020	0.014	0.011	0.011	0.002	0.011	0.006	0.015	0.012	0.012	0.006	0.012
Total	100.2		100.8		100.6		100.4		100.8		100.4	

[a] cpx Compositions within each charge are variable, leading to the high standard deviations. This variability is discussed in Section 3.2.1.

Table 7
Electron microprobe measurements of major elements in experimental garnet and spinel.

	A784	s.d.	A806	s.d.	A825	s.d.	A834	s.d.	A847	s.d.
n	15		14		15		13		17	
Phase	grt		spl		grt		grt		grt	
SiO_2	41.31	0.15	0.384	0.016	42.29	0.09	42.04	0.17	42.0	0.5
TiO_2	0.92	0.13	0.33	0.03	0.82	0.05	0.73	0.08	0.79	0.10
Al_2O_3	23.7	0.2	66.27	0.16	23.94	0.14	23.86	0.18	24.0	0.4
Cr_2O_3	0.30	0.04	1.31	0.08	0.42	0.03	0.57	0.04	0.45	0.06
FeO*	5.96	0.12	8.03	0.11	5.67	0.08	6.72	0.13	6.87	0.13
MnO	0.17	0.02	0.062	0.013	0.180	0.018	0.17	0.02	0.172	0.016
MgO	20.66	0.18	22.92	0.15	21.52	0.11	20.7	0.4	20.4	0.3
CaO	5.6	0.3	0.027	0.015	5.33	0.12	5.6	0.4	5.6	0.4
Na_2O	0.03	0.02	0.011	0.013	0.024	0.016	0.03	0.02	0.04	0.02
K_2O	0.004	0.013	0.002	0.012	0.003	0.011	0.006	0.013	0.004	0.010
Total	98.7		99.35		100.20		100.4		100.4	
D_{Ti}	0.26	0.04	0.099	0.010	0.274	0.017	0.25	0.03	0.24	0.03
D_{Cr}	10	6	40	39	11	7	11.2	1.0	22	5
D_{Mn}	1.3	0.4	0.40	0.11	1.4	0.2	1.17	0.17	1.20	0.12
D_{Fe}	0.712	0.017	0.905	0.015	0.703	0.013	0.664	0.014	0.630	0.016

et al., 2011). We will demonstrate in the following section that differences in mineral composition can have a significant effect on mineral/melt partition coefficients but not mineral/melt exchange coefficients for the divalent FRTE.

The exchange coefficient between two phases, *a* and *b*, is given as:

$$K_D^{i-j} = [X_i^a X_j^b]/[X_j^a X_i^b] \quad (1)$$

where *X* is the molar proportion of element *i* or *j* in phase *a* or *b*. The exchange coefficient can also be calculated as the ratio of two partition coefficients ($K_D^{i-j} = D_i^{a/b}/D_j^{a/b}$), and can be displayed graphically by plotting measurements of the two partition coefficients against each other. If the data fall on a line that passes through the origin, then K_D^{i-j} is given by the slope of that line.

It is important to note that although mineral/melt exchange of divalent FRTE can be considered constant (e.g., Le Roux et al., 2010, 2011), bulk residue/melt exchange coefficients cannot. Bulk residue/melt K_D for two elements *i* and *j* can be calculated from:

$$K_D^{i-j} = \frac{\bar{D}_i}{\bar{D}_i} = \frac{\sum_A W_A D_i^{A/liq}}{\sum_A W_A D_j^{A/liq}} \quad (2)$$

where $\bar{D}_i$ and $\bar{D}_j$ are the bulk residue/melt partition coefficients for elements i and j, W_A is the weight proportion of each mineral A in the residue, and $D_i^{A/liq}$ and $D_j^{A/liq}$ are mineral/melt partition coefficients for i and j for each residual mineral A. Because bulk K_D depends only on individual mineral/melt D and mineral mode, a mineral with a large D has significant leverage over bulk exchange even if it is a small part of the residual mode. For example, average $D_{Mn}^{grt/melt} = 4.64$ and $D_{Fe}^{grt/melt} = 2.51$ during eclogite partial melting (Pertermann et al., 2004) are nearly four times greater than partition coefficients measured in this study ($D_{Mn}^{grt/melt} = 1.24$ and $D_{Fe}^{grt/melt} = 0.65$). Use of these eclogitic garnet partition coefficients led Le Roux et al. (2011) to overestimate bulk garnet peridotite K_D^{Mn-Fe} at 1.21 ± 0.04, whereas we calculate $K_D^{Mn-Fe} = 1.03 \pm 0.02$ from the same residual mode (Walter, 1998) but using our mineral/melt partition coefficients. Despite near-constant values of divalent FRTE mineral/melt K_D, compositionally-appropriate values of mineral/melt partition coefficients must be used to calculate bulk K_D in partial melting models.

The constancy of some mineral/melt exchange coefficients over wide ranges of pressure, temperature, and composition can be used to estimate partition coefficients under conditions that have not been explored experimentally. For example, given knowledge of a particular mineral/melt D_{Fe}, mineral/melt partition coefficients for the other divalent FRTE can be deduced.

4.2. Comparison to previous measurements of FRTE partitioning

Fe and Mn: Fe and Mn are routinely measured in partial melting experiments, providing a collection of measurements made over a large range of pressures, temperatures, and compositions for comparison. $D_{Mn}^{min/melt}$ is inversely correlated with temperature for all peridotite minerals (Fig. 4). As noted by Balta et al. (2011), the temperature dependence of $D_{Mn}^{min/melt}$ for peridotite minerals is less pronounced than for eclogite minerals; this is particularly evident in garnet (Fig. 4). Fig. 5 shows that $D_{Mn}^{min/melt}$ is strongly correlated with mineral Mg#. For cpx and garnet this correlation is approximately linear, suggesting that composition, not temperature, is the dominant control on Mn partitioning.

As described in Section 4.1, D_{Fe} and D_{Mn} compiled from several peridotite and eclogite partial melting studies (Fig. 6) demonstrate that K_D^{Mn-Fe} between mantle minerals and melt is insensitive to temperature (1201–1950 °C), pressure (100 kPa–7 GPa), and composition (Mg#: 0.80–0.95). K_D^{Mn-Fe} is <1 in olivine and >1 in cpx, opx, and garnet. This means that olivine in a melting residue tends to drive the coexisting melt to lower Fe/Mn while the other residual minerals in a garnet peridotite tend to drive the melt composition to higher Fe/Mn (Humayun et al., 2004; Le Roux et al., 2011).

Bulk K_D^{Mn-Fe} for garnet peridotite near its solidus is ~1; using our average partition coefficients (Table 13), near-solidus partial melting of garnet peridotite KLB-1ox (Davis et al., 2011) at 3 GPa has a bulk $K_D^{Mn-Fe} = 0.96 \pm 0.02$. This means that near-solidus melts of garnet peridotite will inherit Fe/Mn approximately equal to that of their source, and this will be the maximum Fe/Mn that can be achieved by melts derived from that source. $\bar{D}_{Mn}$ and bulk K_D^{Mn-Fe} decrease with increasing melt fraction and decreasing proportion of garnet and cpx in the residue, leading to a decrease in Fe/Mn of higher degree melts.

In Section 4.1, we demonstrated that the use of compositionally inappropriate $D_{Mn}^{grt/melt}$ and $D_{Fe}^{grt/melt}$ leads to an overestimation of bulk peridotite K_D^{Mn-Fe}. Using eclogitic garnet partition coefficients, Le Roux et al. (2011) calculated a near-solidus partial melt of peridotite with Fe/Mn = 72.4 derived from a source with Fe/Mn = 59.9 (PUM, McDonough and Sun, 1995). This is much higher than can actually be achieved using peridotite mineral/melt partition coefficients from this study, which give a near-solidus melt with Fe/Mn = 61.7 using the same residual mode and source composition ($K_D^{Mn-Fe} = 1.03 \pm 0.02$).

Zn: Like Mn/Fe ratios, Zn/Fe may be minimally fractionated during peridotite partial melting, so Zn/Fe ratios in basalt different from ratios found in peridotite may indicate recycled crust in the OIB source region (Le Roux et al., 2010, 2011). Experimental measurements of D_{Zn} remain sparse, but our measurements combined with those of Pertermann et al. (2004) and Le Roux et al. (2011) show that there is a nearly linear increase in D_{Zn} with decreasing Mg#. In detail, our measured values of D_{Zn} for cpx and garnet are less than those found by Pertermann et al. (2004), and for all peridotite phases, the new 3 GPa data are less than those found at 1.5 GPa from more Fe-enriched experiments (Le Roux et al., 2011); however, the 3 GPa measurements of $D_{Zn}^{ol/melt}$ are similar to those measured at 2 GPa by Le Roux et al. (2011) at similar Mg#.

Fig. 6 shows that K_D^{Zn-Fe} for each mineral–melt pair is constant over the experimental conditions explored, although there is considerably more scatter for olivine than for other minerals. K_D^{Zn-Fe} is less than unity for all phases, which means that partial melts of garnet peridotite will have higher Zn/Fe than their source. We calculate bulk $K_D^{Zn-Fe} = 0.84$ and $(\text{Zn/Fe}) * 10^4 = 10.4$ for a near-solidus melt of KLB-1ox at 3 GPa. Le Roux et al. (2011) also found $K_D^{Zn-Fe} < 1$ for all mineral–melt pairs, but predicted a lower bulk peridotite $K_D^{Zn-Fe} = 0.73$ and higher melt $(\text{Zn/Fe}) * 10^4 = 11.3$ owing to their use of eclogitic garnet and cpx partition coefficients. It is notable that $D_{Zn}^{spl/melt}$ (5.2 ± 0.5) is significantly greater than any of the other peridotite mineral/melt partition coefficients, and a peridotite with small amounts of spinel will have a larger K_D^{Zn-Fe} (e.g., $K_D^{Zn-Fe} = 0.99$ for near solidus melting of a spinel peridotite with the mineral mode of KLB-1, Davis et al., 2009).

Co: Co/Fe is another potential tracer of basalt source lithology (Le Roux et al., 2011). Like the exchange behavior of other divalent FRTE, K_D^{Co-Fe} is constant over the pressure (1.5–3 GPa) and temperature (1300–1470 °C) interval where data are available (Fig. 6). For all phases $D_{Co} > D_{Fe}$, so melt Co/Fe will always be less than Co/Fe in the source lithology. Our measurement of $D_{Co}^{ol/melt}$ agrees well with those from the 2 GPa experiments of Le Roux et al. (2011), and our more magnesian cpx and garnet have smal-

Table 8
LA-ICP-MS measurements of major and trace elements in experimental melt.

	A779	s.d.	A781	s.d.	A784	s.d.	A786	s.d.	A788	s.d.	A791	s.d.	A799	s.d.
n	438		276		13		483		524		198		6	
SiO_2	45.6	1.2	40.5	1.4	44.1	1.2	41.6	1.1	43.2	1.1	42.9	0.6	47.0	0.8
TiO_2	3.09	0.12	3.72	0.17	3.77	0.06	3.52	0.16	3.78	0.15	3.49	0.10	2.73	0.06
Al_2O_3	12.9	0.5	14.2	0.5	11.8	0.6	13.6	0.5	13.9	0.4	13.3	0.3	12.00	0.18
FeO^*	8.7	0.6	10.2	0.6	8.2	0.3	9.0	0.4	9.5	0.4	7.9	0.2	8.93	0.07
MnO	0.149	0.011	0.170	0.010	0.153	0.006	0.157	0.007	0.154	0.006	0.156	0.004	0.149	0.002
MgO	15.5	0.6	15.9	0.8	15.9	0.3	16.1	0.7	14.3	0.6	15.8	0.5	14.9	0.3
CaO	10.3	0.4	10.2	0.4	10.6	0.4	10.9	0.4	9.8	0.4	11.3	0.3	8.92	0.18
Na_2O	2.6	0.3	3.3	0.5	3.6	0.3	3.51	0.18	3.5	0.2	3.50	0.10	3.80	0.07
K_2O	1.20	0.13	1.66	0.12	1.80	0.09	1.62	0.09	1.77	0.10	1.59	0.05	1.60	0.02
P2O5	0.017	0.002	0.021	0.003	0.021	0.002	0.017	0.004	0.021	0.004	0.020	0.003	0.010	0.008
Total	100		100		100		100		100		100		100	
Sc	84	3	91	4	57	2	93	5	92	4	96	4	71.8	1.5
V	57	3	58	4	47	2	61	3	52	4	56	2	53.9	0.7
Cr	460	30	350	60	200	18	420	30	350	70	320	60	462	6
Co	49	12	45	2	36.6	1.4	40	2	32	3	29	2	27.8	0.6
Zn	130	40	150	20	111	12	121	8	139	11	116	10	123	3
Ga	81	5	103	5	93	3	111	7	116	7	96	4	106	2
Ge	62	3	74	4	47.9	1.5	75	4	73	5	62	4	79.0	1.7

	A806	s.d.	A825	s.d.	A830	s.d.	A834	s.d.	A842	s.d.	A847	s.d.
n	714		6		816		650		778		183	
SiO_2	42.5	1.2	48.2	0.3	43.3	1.0	43.4	1.0	43.7	1.4	43.1	1.6
TiO_2	3.9	0.2	3.07	0.04	3.04	0.12	3.52	0.12	2.85	0.12	3.76	0.18
Al_2O_3	13.9	0.5	12.38	0.14	14.1	0.4	12.7	0.6	15.0	0.5	12.4	0.6
FeO^*	8.2	0.4	7.10	0.05	7.6	0.3	9.5	0.4	9.3	0.5	10.1	0.6
MnO	0.160	0.009	0.144	0.001	0.160	0.007	0.162	0.012	0.158	0.012	0.16	0.02
MgO	15.0	0.6	13.99	0.11	16.6	0.7	15.8	0.7	15.4	0.8	14.6	0.9
CaO	10.5	0.5	9.08	0.09	10.8	0.4	10.0	0.3	9.6	0.4	9.9	0.4
Na_2O	3.8	0.2	4.18	0.03	3.0	0.3	3.0	0.4	2.8	0.3	3.7	0.5
K_2O	2.0	0.2	1.804	0.015	1.36	0.13	1.72	0.17	1.3	0.2	2.2	0.3
P2O5	0.018	0.004	0.023	0.003	0.016	0.005	0.018	0.016	0.018	0.008	0.037	0.013
Total	100		100		100		100		100		100	
Sc	85	5	44.0	0.8	87	4	48	3	90	5	35	3
V	47	3	42.7	0.4	58	3	54	4	55	4	46	5
Cr	190	40	279	5	840	90	540	150	900	100	260	60
Co	27	5	31.5	0.4	32	2	37	2	31	3	43	3
Zn	123	11	119.4	1.5	135	12	159	17	151	16	210	30
Ga	90	7	94.3	0.8	85	5	116	6	104	7	128	14
Ge	60	5	58.1	1.5	57	4	69	4	72	5	62	5

ler D_{Co} than those presented in Pertermann et al. (2004) and Le Roux et al. (2011). Bulk K_D^{Co-Fe} is 2.15 ± 0.07 for a near-solidus melt of garnet peridotite (KLB-1ox) at 3 GPa.

Ga and Sc: The trivalent cations Ga and Sc might be expected to behave similarly during partial melting of peridotite as they have similar compatibilities in olivine and pyroxenes (Fig. 3); however, D_{Ga} is strongly stabilized by Al_2O_3 in pyroxenes, whereas the correlation between D_{Sc} and Al_2O_3 is less clear (Figs. 7–9). The different behavior of these elements is likely related to the larger cation radius of Sc^{3+} (0.745 Å in octahedral coordination, Shannon, 1976) compared to Ga^{3+} (0.62 Å), which is closer in size to Al^{3+} (0.535 Å). D_{Ga} and D_{Al} for olivine, opx, and cpx depend upon each other linearly (Fig. 7–9) giving constant values of K_D^{Ga-Al}. This suggests that D_{Ga}^{cpx} can be estimated in systems where Ga partitioning is less well-constrained (i.e., eclogite partial melting) given knowledge of D_{Ga}^{cpx}. Unfortunately, a similar relation for K_D^{Sc-Al} is not evident in any of the peridotite minerals.

The distinct partitioning behavior of Sc and Ga in garnet and spinel may also be related to differences in ionic radii. Sc is highly compatible in garnet (Fig. 3), and Ga is moderately incompatible. This may be because Sc^{3+} has an 8-fold coordinated ionic radius near optimum for the garnet X-site (van Westrenen et al., 1999), while Ga^{3+} goes into the Y-site where it is larger than the primary occupant, Al^{3+}. In spinel, Ga is highly compatible and Sc is mildly incompatible. Ga^{3+} is intermediate in size between Mg^{2+} and Al^{3+} and likely resides in both octahedral and tetrahedral sites. In contrast, Sc^{3+} is large compared to the octahedral site of spinel. Because garnet fractionates Ga and Sc efficiently, melts formed in the presence of residual garnet are expected to have elevated Ga/Sc compared with their source. Residual spinel would be expected to lower Ga/Sc ratios of coexisting melts.

Table 9
LA-ICP-MS measurements of major and trace elements in experimental olivine.

	A779	s.d.	A781	s.d.	A784	s.d.	A786	s.d.	A788	s.d.	A791	s.d.
n	2		3		2		3		5		305	
SiO_2 (wt.%)	41.9	0.2	40.24	0.10	42.2	0.4	39.37	0.15	40.7	0.4	41.6	0.6
TiO_2	0.0172	0.0011	0.026	0.012	0.032	0.005	0.021	0.004	0.031	0.007	0.0140	0.0013
Al_2O_3	0.18	0.05	0.21	0.06	0.186	0.014	0.158	0.016	0.22	0.03	0.122	0.004
FeO*	8.17	0.07	9.8	0.4	8.6	0.2	9.231	0.006	9.9	0.3	5.70	0.16
MnO	0.1095	0.0010	0.121	0.003	0.120	0.004	0.1208	0.0007	0.1242	0.0008	0.085	0.002
MgO	49.3	0.2	48.8	0.3	48.5	0.6	50.82	0.09	48.4	0.3	52.3	0.6
CaO	0.25	0.03	0.27	0.06	0.264	0.016	0.254	0.014	0.25	0.04	0.217	0.009
Na_2O	0.035	0.005	0.480	0.016	0.069	0.006	0.01	0.05	0.26	0.14	nd	
K_2O	0.002	0.002	nd		0.014	0.008	0.005	0.003	0.004	0.005	nd	
P2O5	0.0080	0.0010	0.0055	0.0003	0.0053	0.0006	0.0053	0.0008	0.008	0.002	0.006	0.003
Total	100		100		100		100		100		100	
K_D^{Fe-Mg}	0.29		0.31		0.35		0.32		0.31		0.22	
Sc (ppm)	10.8	0.3	11.6	0.7	8.9	0.7	12.2	0.3	11.7	0.7	9.0	0.7
V	9.2	0.6	6.9	0.3	6.6	0.2	7.07	0.07	6.5	0.4	7.8	0.6
Cr	408	6	230	60	230	80	270	20	220	12	510	30
Co	100	20	95.5	0.4	85	3	89	2	85	5	57	3
Zn	103	3	124	5	112	9	115	2	151	10	72	7
Ga	1.77	0.04	2.5	0.3	2.66	0.04	2.45	0.18	3.2	0.2	1.5	0.3
Ge	25.6	1.4	26.9	1.0	22.9	0.5	26.4	1.3	28.4	0.8	23	2
D_{Sc}	0.128	0.006	0.127	0.009	0.156	0.013	0.131	0.007	0.127	0.010	0.093	0.009
D_{Ti}	0.0056	0.0004	0.007	0.003	0.0084	0.0014	0.0059	0.0012	0.008	0.002	0.0040	0.0004
D_V	0.162	0.015	0.120	0.009	0.142	0.007	0.116	0.007	0.124	0.012	0.139	0.012
D_{Cr}	0.88	0.05	0.64	0.19	1.1	0.4	0.65	0.07	0.62	0.13	1.6	0.3
D_{Mn}	0.73	0.05	0.71	0.05	0.78	0.04	0.77	0.03	0.81	0.03	0.55	0.02
D_{Fe}	0.94	0.06	0.96	0.07	1.05	0.04	1.02	0.04	1.05	0.05	0.72	0.03
D_{Co}	2.1	0.7	2.14	0.10	2.32	0.13	2.21	0.13	2.7	0.3	1.98	0.15
D_{Zn}	0.8	0.3	0.82	0.12	1.01	0.13	0.94	0.07	1.09	0.11	0.62	0.08
D_{Ga}	0.022	0.001	0.024	0.003	0.0287	0.0010	0.022	0.002	0.027	0.002	0.015	0.004
D_{Ge}	0.41	0.03	0.36	0.02	0.479	0.018	0.35	0.03	0.39	0.03	0.38	0.04

	A799	s.d.	A806	s.d.	A825	s.d.	A830	s.d.	A834	s.d.	A842	s.d.
n	2		19		2		5		4		7	
SiO_2	39.88	0.06	41.34	0.17	42.9	0.5	40.8	0.3	40.6	0.2	40.2	0.9
TiO_2	0.021	0.003	0.017	0.003	0.033	0.012	0.0170	0.0005	0.046	0.013	0.021	0.004
Al_2O_3	0.165	0.013	0.172	0.017	0.33	0.08	0.159	0.004	0.24	0.04	0.19	0.05
FeO*	9.3	0.4	7.1	0.8	8.13	0.19	8.08	0.10	9.77	0.04	9.72	0.19
MnO	0.122	0.004	0.104	0.009	0.128	0.004	0.1216	0.0007	0.1215	0.0003	0.124	0.002
MgO	50.2	0.4	51.0	0.8	48.0	0.5	50.5	0.2	48.64	0.12	49.4	0.7
CaO	0.234	0.003	0.215	0.007	0.40	0.10	0.228	0.003	0.31	0.03	0.24	0.04
Na_2O	0.061	0.013	0.07	0.04	0.093	0.014	0.15	0.03	0.23	0.02	0.08	0.04
K_2O	nd		0.003	0.005	0.0034	0.0014	0.0009	0.0011	0.017	0.009	nd	
P2O5	nd		0.0052	0.0006	nd		0.0041	0.0014	0.0067	0.0007	0.004	0.002
Total	100		100		100		100		100		100	
K_D^{Fe-Mg}	0.31		0.25		0.33		0.35		0.33		0.33	
Sc	11.8	0.3	9.9	0.6	11.9	0.7	10.79	0.13	6.68	0.17	11.6	0.5
V	7.3	0.4	7.7	1.4	7.36	0.09	7.52	0.16	8.1	0.3	8.4	0.3
Cr	370	60	600	170	450	80	440	30	247	16	510	20
Co	67	5	68	4	88	5	79	3	83	2	72	3
Zn	125	6	102	11	116	3	129.9	1.7	159	4	144	5
Ga	2.6	0.3	2.2	0.4	3.0	0.3	2.00	0.07	3.9	0.4	2.4	0.4
Ge	35.9	0.5	26.1	0.8	34.1	0.5	28.0	0.7	22	5	9	8
D_{Sc}	0.164	0.006	0.117	0.011	0.271	0.016	0.124	0.005	0.140	0.011	0.129	0.009
D_{Ti}	0.0079	0.0010	0.0044	0.0007	0.011	0.004	0.0056	0.0003	0.013	0.004	0.0072	0.0014
D_V	0.136	0.007	0.16	0.03	0.172	0.003	0.129	0.008	0.151	0.013	0.152	0.011
D_{Cr}	0.80	0.13	3.1	1.1	1.6	0.3	0.53	0.07	0.46	0.13	0.56	0.07
D_{Mn}	0.81	0.03	0.65	0.07	0.89	0.03	0.76	0.03	0.75	0.06	0.78	0.06

(*continued on next page*)

Table 9 (*continued*)

	A799	s.d.	A806	s.d.	A825	s.d.	A830	s.d.	A834	s.d.	A842	s.d.
D_{Fe}	1.04	0.05	0.87	0.10	1.15	0.03	1.06	0.04	1.03	0.05	1.05	0.06
D_{Co}	2.4	0.2	2.5	0.5	2.78	0.16	2.5	0.2	2.22	0.13	2.3	0.3
D_{Zn}	1.02	0.06	0.83	0.12	0.98	0.03	0.96	0.09	1.00	0.11	0.95	0.11
D_{Ga}	0.024	0.002	0.025	0.005	0.032	0.003	0.0235	0.0017	0.034	0.004	0.023	0.004
D_{Ge}	0.455	0.012	0.43	0.04	0.587	0.018	0.49	0.03	0.32	0.07	0.12	0.11

nd = not detected.

Using our estimates of D_{Ga} and D_{Al}, we predict near-solidus partial melting of garnet peridotite with the mineral mode of KLB-1ox at 3 GPa has a bulk $K_D^{Ga-Al} = 0.49 \pm 0.05$. A near-solidus melt of such a peridotite, assuming Ga and Al contents of PUM (McDonough and Sun, 1995), will have a $(Ga/Al) * 10^4 = 3.6$, similar to the upper range of Ga/Al ratios found in alkalic OIB (see Section 4.3 for details of the OIB dataset).

V: Multivalent V may be useful as a probe of f_{O2} of magma source regions (e.g., Shervais, 1982; Canil, 1997; Lee et al., 2005). Because V^{4+} and V^{5+} are incompatible in all mantle minerals, D_V decreases at high f_{O2} causing ratios in melts such as V/Ti (Shervais, 1982) and V/Sc (Lee et al., 2005) to increase. The influence of f_{O2} on V partitioning between melts and mantle mineral phases has been studied over a range of pressures and temperatures (Canil, 1997, 1999; Canil and Fedortchouk, 2000, 2001; Mallmann and O'Neill, 2009), and Mallmann and O'Neill (2009) developed a model to predict the compatibility of V in olivine, opx, cpx, and spinel based on experiments from 100 kPa to 1 GPa. The effects of pressure and temperature on V partitioning appear to be minor compared to the influence of f_{O2} (Canil and Fedortchouk, 2000, 2001).

Our measurements of D_V in experiments that included Pt-Fe can be compared with other experimental D_V at similar f_{O2}. To compare our results to other studies we calculate f_{O2} of the experiments relative to the quartz-fayalite-magnetite (QFM) buffer at the pressure and temperature conditions of the experiment. For experiments at pressures >100 kPa we determine QFM following the pressure-dependent calibration of Frost (1991), and we calculate QFM at 100 kPa following (O'Neill, 1987) to remain consistent with the presentation of the model of Mallmann and O'Neill (2009). Measurements of D_V^{ol} and D_V^{cpx} from our experiments plotted against ΔQFM are in close agreement with the models of Mallmann and O'Neill (2009) and other experimental measurements at 100 kPa and 1 GPa (Fig. 10, Canil, 1997; Canil and Fedortchouk, 2000, 2001; Mallmann and O'Neill, 2009). In contrast, Mallmann and O'Neill (2009) note that their experiments at 3 GPa display D_V^{cpx} systematically higher than those predicted by their model. This may be due to an overestimation of f_{O2} in these experiments, for which f_{O2} was determined from the solubility of Re in melt, calibrated at 100 kPa and 1400 °C (Mallmann and O'Neill, 2007).

Ge: It has been observed that Ga/Ge in OIB is systematically higher than in MORB (Arevalo and McDonough, 2010b). Ge is not analyzed routinely in natural basalts or peridotites, and experimental measurements of Ge partitioning are rare. Hill et al. (2000) found that their cpx contained <10 ppm of Ge allowing them to present measurements of D_{Ge}^{cpx}. Adam and Green (2006) included Ge among the suite of elements used to dope hydrous peridotite partial melting experiments and presented measurements of D_{Ge} for olivine, opx, and cpx. D_{Ge}^{cpx} displays a weak inverse correlation with temperature, and notably, there is no correlation between D_{Ge}^{cpx} and SiO_2 (Fig. 11). To our knowledge, the measurement of D_{Ge}^{grt} in this study is the only published experimental value. Ge is mildly incompatible in all the phases we have analyzed, except garnet (Table 13), and the near-solidus bulk $\bar{D}_{Ge} = 0.66 \pm 0.01$ for garnet peridotite with mineral mode of KLB-1ox at 3 GPa.

4.3. Partial melting model and FRTE ratios in OIB

Our average mineral/melt partition coefficients are used to derive bulk peridotite/melt partition coefficients and model melt compositions that can be compared to natural OIB. We present a simple model of peridotite partial melting that simulates isobaric, modal batch melting of fertile peridotite at 3 GPa. Of course, actual melting in the mantle is polybaric, but this simple model is sufficient to explore the compositional effects of varying the residual mineralogy of fertile peridotite residues that may contribute to melting beneath oceanic lithosphere over a range of melt fractions. Three different starting compositions were considered: primitive upper mantle (PUM) as estimated by McDonough and Sun (1995) and two fertile peridotite xenoliths, Ki5-8b (Lee, 2005) and RP87-2 (Zangana et al., 1999, Table 14). These two xenoliths are the most fertile compositions from two detailed regional studies of continental xenoliths, as determined by their Al_2O_3 contents (Lee, 2005). Each of these compositions falls within the range defined by peridotite xenoliths found in the GEOROC database (http://georoc.mpchmainz.gwdg.de/georoc/, accessed 04/13/2011). Melt fractions and corresponding modes are tied to peridotite partial melting experiments (Walter, 1998; Davis et al., 2011).

Key FRTE ratios of model partial melts of peridotite are presented in Figs. 12 and 13. The right side of the panels of Fig. 12 show a trend of increasing melt fraction for a garnet lherzolite with the initial mineral mode of KLB-1ox at its solidus at 3 GPa (Davis et al., 2011). The effects of increasing melt fraction and changing residual mode are not easily deconvolved, so we have also calculated a near-solidus melt composition without garnet in the residue (relative proportions of ol, opx, and cpx held constant). This allows us to

Table 10
LA-ICP-MS measurements of major and trace elements in experimental opx.

	A784	s.d.	A786	s.d.	A788	s.d.	A791	s.d.	A799	s.d.
n	10		131		2		174		2	
SiO_2 (wt.%)	56.6	0.9	52.4	0.8	56.2	0.3	55.4	0.7	56.6	0.2
TiO_2	0.2	0.0	0.25	0.03	0.175	0.009	0.195	0.011	0.190	0.008
Al_2O_3	4.02	0.18	4.7	0.2	3.7	0.5	4.39	0.12	4.83	0.04
FeO*	4.19	0.13	4.8	0.3	4.71	0.17	3.76	0.13	4.75	0.07
MnO	0.092	0.002	0.101	0.004	0.099	0.001	0.088	0.003	0.098	0.002
MgO	32.4	0.7	34.4	0.8	31.90	0.01	33.7	0.7	31.16	0.08
CaO	2.25	0.07	3.09	0.16	2.53	0.05	2.29	0.08	2.07	0.16
Na_2O	0.25	0.03	0.29	0.05	0.679	0.004	0.20	0.02	0.3679	0.0004
K_2O	0.01	0.01	0.01	0.01	0.02	0.01	nd		nd	
P_2O_5	0.008	0.001	0.006	0.003	0.010	0.001	0.006	0.003	nd	
Total	100		100		100		100		100	
Sc (ppm)	32.6	1.0	41.8	1.7	29	3	36	2	35.2	1.7
V	43.2	0.8	55	3	45	6	46	2	55.0	0.6
Cr	2100	50	2460	160	2200	300	2300	90	2850	60
Co	38.9	0.8	41	2	70	40	27.4	1.8	30.44	0.09
Zn	42	3	51	5	68.1	0.8	43	4	58.6	0.4
Ga	20.7	0.8	27	2	25	2	22.4	1.5	32.19	0.12
Ge	47.3	1.8	59	3	55	2	49	3	68.3	0.2
D_{Sc}	0.57	0.03	0.45	0.03	0.31	0.03	0.38	0.03	0.49	0.03
D_{Ti}	0.048	0.003	0.070	0.008	0.046	0.003	0.056	0.003	0.070	0.003
D_V	0.93	0.04	0.91	0.07	0.86	0.14	0.83	0.05	1.020	0.018
D_{Cr}	10.5	1.0	5.8	0.5	6.3	1.6	7.2	1.4	6.18	0.15
D_{Mn}	0.60	0.03	0.64	0.04	0.65	0.03	0.57	0.02	0.659	0.014
D_{Fe}	0.51	0.02	0.53	0.04	0.50	0.03	0.48	0.02	0.531	0.009
D_{Co}	1.06	0.05	1.03	0.08	2.2	1.2	0.95	0.08	1.10	0.02
D_{Zn}	0.38	0.05	0.42	0.05	0.49	0.04	0.37	0.05	0.476	0.011
D_{Ga}	0.223	0.011	0.24	0.02	0.22	0.02	0.234	0.019	0.304	0.006
D_{Ge}	0.99	0.05	0.78	0.06	0.76	0.06	0.80	0.07	0.865	0.019

	A806	s.d.	A825	s.d.	A830	s.d.	A842	s.d.
n	19		2		288		43	
SiO_2	54.2	1.6	57.5	0.8	52.8	0.7	50.3	0.7
TiO_2	0.21	0.02	0.189	0.018	0.249	0.017	0.294	0.012
Al_2O_3	6.1	0.4	5.4	0.3	6.0	0.4	9.3	0.2
FeO*	3.9	0.3	4.49	0.17	4.83	0.13	5.73	0.14
MnO	0.092	0.006	0.0982	0.0007	0.106	0.004	0.114	0.003
MgO	33.0	1.4	30.1	1.1	33.0	0.6	31.5	0.7
CaO	2.21	0.11	1.91	0.01	2.64	0.13	2.40	0.06
Na_2O	0.24	0.02	0.34	0.04	0.27	0.03	0.31	0.03
K_2O	nd		0.00	0.01	0.006	0.004	0.002	0.002
P_2O_5	0.002	0.002	nd		0.006	0.004	0.008	0.005
Total	100		100		100		100	
Sc	35	3	33.1	1.0	42	3	55	2
V	55	4	55	2	70	3	75	3
Cr	3800	300	3970	100	4100	200	3640	110
Co	30	3	48	3	47	3	33	2
Zn	47	6	52	3	70	6	88	8
Ga	28	3	28	2	31	2	51	4
Ge	49	4	59	3	54	3	63	4
D_{Sc}	0.41	0.04	0.75	0.03	0.48	0.04	0.61	0.04
D_{Ti}	0.054	0.007	0.062	0.006	0.082	0.006	0.103	0.006
D_V	1.17	0.11	1.29	0.06	1.19	0.09	1.35	0.10
D_{Cr}	20	4	14.2	0.4	4.9	0.6	4.1	0.4
D_{Mn}	0.58	0.05	0.682	0.007	0.66	0.04	0.73	0.06
D_{Fe}	0.48	0.05	0.63	0.02	0.64	0.03	0.62	0.03
D_{Co}	1.1	0.2	1.54	0.10	1.48	0.15	1.07	0.14
D_{Zn}	0.38	0.06	0.43	0.03	0.51	0.07	0.59	0.08
D_{Ga}	0.32	0.04	0.294	0.018	0.36	0.04	0.49	0.05
D_{Ge}	0.81	0.10	1.01	0.06	0.95	0.08	0.88	0.08

Table 11
LA-ICP-MS measurements of major and trace elements in experimental cpx.

	A779	s.d.	A781	s.d.	A784	s.d.	A786	s.d.	A788	s.d.	A791	s.d.	A799	s.d.
n	371		629		647		178		511		210		89	
SiO_2 (wt.%)	54.33	0.07	51.10	0.04	55.02	0.15	50.55	0.05	52.71	0.06	52.64	0.09	55.2	0.9
TiO_2	0.3646	0.0014	0.415	0.001	0.354	0.008	0.380	0.002	0.429	0.009	0.433	0.003	0.37	0.03
Al_2O_3	6.21		6.83		5.66		6.52		6.66		6.39		6.8	0.5
FeO^*	4.259	0.014	4.460	0.010	3.81	0.03	4.270	0.020	4.710	0.020	3.90	0.02	4.1	0.2
MnO	0.1157	0.0004	0.1166	0.0002	0.116	0.001	0.1194	0.0005	0.1208	0.0004	0.117	0.000	0.111	0.005
MgO	22.39	0.08	24.83	0.04	23.88	0.12	25.14	0.06	22.59	0.06	24.03	0.08	21.8	1.0
CaO	11.27	0.04	11.06	0.02	10.17	0.05	11.94	0.04	11.55	0.04	11.29	0.03	10.4	0.8
Na_2O	1.043	0.006	1.161	0.003	0.97	0.02	1.073	0.007	1.214	0.006	1.16	0.01	1.24	0.09
K_2O	0.0077	0.0004	0.023	0.001	0.031	0.004	0.0020	0.0005	0.011	0.006	0.044	0.001	0.005	0.003
P_2O_5	0.0070	0.0001	0.0068	0.0001	0.0062	0.0002	0.0063	0.0006	0.0046	0.0003	0.015	0.006	0.01	0.01
Total	100		100		100		100		100		100		100	
Sc (ppm)	61.2	0.2	60.4	0.1	56.8	0.3	70.7	0.4	69.0	0.2	65.6	0.2	61	4
V	76.4	0.2	76.6	0.2	64.9	0.4	82.2	0.4	78.6	0.4	70.9	0.3	75	5
Cr	2132	16	2212	7	2360	20	2740	20	2152	11	2361	14	2370	170
Co	27.88	0.16	33.3	0.1	26.3	0.6	31.0	0.2	31.6	0.2	21.3	0.1	21	1
Zn	35.3	0.3	41.7	0.2	31.6	1.0	42.0	0.6	46.3	0.5	42.7	0.8	44	4
Ga	28.38	0.13	32.4	0.1	25.9	0.3	35.1	0.3	39.1	0.3	31.4	0.4	36	4
Ge	52.3	0.2	61.3	0.2	46.6	0.4	65.9	0.5	63.4	0.3	60.0	0.6	66	5
D_{Sc}	0.73	0.03	0.66	0.03	1.00	0.04	0.76	0.04	0.75	0.03	0.68	0.03	0.85	0.06
D_{Ti}	0.118	0.004	0.111	0.005	0.094	0.003	0.108	0.005	0.113	0.005	0.124	0.004	0.136	0.012
D_V	1.35	0.08	1.33	0.08	1.39	0.06	1.35	0.07	1.51	0.10	1.27	0.06	1.39	0.09
D_{Cr}	4.6	0.3	6.3	1.1	11.8	1.1	6.5	0.4	6.1	1.3	7.3	1.4	5.1	0.4
D_{Mn}	0.78	0.06	0.69	0.04	0.76	0.03	0.76	0.03	0.79	0.03	0.75	0.02	0.75	0.03
D_{Fe}	0.49	0.03	0.44	0.03	0.465	0.015	0.47	0.02	0.50	0.02	0.493	0.013	0.46	0.02
D_{Co}	0.57	0.14	0.74	0.04	0.72	0.03	0.77	0.04	0.99	0.08	0.74	0.04	0.76	0.05
D_{Zn}	0.27	0.09	0.27	0.04	0.29	0.03	0.35	0.02	0.33	0.03	0.37	0.03	0.36	0.03
D_{Ga}	0.35	0.02	0.315	0.017	0.280	0.009	0.32	0.02	0.34	0.02	0.329	0.016	0.34	0.03
D_{Ge}	0.84	0.04	0.82	0.04	0.97	0.03	0.87	0.05	0.87	0.06	0.97	0.06	0.84	0.07

	A806	s.d.	A825	s.d.	A830	s.d.	A834	s.d.	A842	s.d.	A847	s.d.
n	291		6		127		6		80		6	
SiO_2	53.60	0.20	55.1	0.5	51.0	1.3	51.8	0.7	48.8	1.0	52.6	0.4
TiO_2	0.353	0.010	0.44	0.07	0.44	0.03	0.49	0.14	0.48	0.05	0.48	0.13
Al_2O_3	6.63		8.0	0.4	7.3	0.4	7.1	1.1	8.7	0.5	6.89	0.19
FeO^*	3.58	0.05	4.00	0.11	4.3	0.2	4.7	0.2	4.7	0.2	4.6	0.3
MnO	0.114	0.001	0.125	0.004	0.126	0.006	0.124	0.005	0.130	0.006	0.121	0.004
MgO	23.87	0.18	21.4	0.5	23.9	1.0	22.0	1.1	23.7	1.1	21.9	1.0
CaO	10.59	0.10	9.5	0.4	11.7	0.5	12.0	0.8	12.2	0.4	11.8	1.0
Na_2O	1.19	0.02	1.44	0.13	1.20	0.13	1.69	0.17	1.3	0.2	1.6	0.2
K_2O	0.029	0.007	0.03	0.04	0.04	0.04	0.06	0.09	0.04	0.02	0.04	0.05
P_2O_5	0.0041	0.0006	nd		0.005	0.003	0.007	0.002	0.005	0.003	0.009	0.004
Total	100		100		100		100		100		100	
Sc	51.7	0.7	55.2	1.5	63	4	49	14	71	3	37	6
V	70.8	0.8	71	3	88	6	84	5	99	7	72	6
Cr	3220	80	3200	600	4000	400	2500	500	4000	200	1900	900
Co	36	3	30	3	32	3	33	3	28	5	35	2
Zn	38.0	1.0	43	3	57	7	56	5	56	9	59	6
Ga	33.6	0.6	38	3	36	4	46	6	42	4	48	7
Ge	51.9	0.7	63	3	58	4	52	7	41	10	51	7
D_{Sc}	0.61	0.04	1.26	0.04	0.72	0.05	1.0	0.3	0.79	0.05	1.1	0.2
D_{Ti}	0.090	0.005	0.14	0.02	0.145	0.013	0.14	0.04	0.167	0.017	0.13	0.04
D_V	1.51	0.10	1.67	0.08	1.51	0.13	1.56	0.15	1.80	0.17	1.6	0.2
D_{Cr}	17	3	12	2	4.8	0.6	4.6	1.6	4.4	0.5	7	4
D_{Mn}	0.71	0.04	0.87	0.03	0.79	0.05	0.77	0.06	0.83	0.08	0.76	0.08
D_{Fe}	0.44	0.02	0.563	0.016	0.57	0.04	0.50	0.03	0.51	0.03	0.45	0.04
D_{Co}	1.3	0.3	0.95	0.08	1.03	0.12	0.89	0.09	0.92	0.18	0.80	0.07
D_{Zn}	0.31	0.03	0.36	0.02	0.42	0.06	0.35	0.05	0.37	0.07	0.28	0.05
D_{Ga}	0.37	0.03	0.40	0.04	0.42	0.05	0.40	0.06	0.40	0.05	0.37	0.07
D_{Ge}	0.86	0.08	1.08	0.05	1.01	0.10	0.76	0.12	0.57	0.14	0.82	0.13

Table 12
LA-ICP-MS measurements of major and trace elements in experimental garnet and spinel.

	A784	s.d.	A806	s.d.	A825	s.d.	A834	s.d.	A847	s.d.
n	8		3		5		16		20	
Phase	grt		spl		grt		grt		grt	
SiO_2 (wt.%)	42.2	1.2	0.6	0.2	46.7	0.5	42.6	0.9	42.1	0.7
TiO_2	1.03	0.12	0.33	0.03	0.84	0.03	0.87	0.05	0.97	0.05
Al_2O_3	23.6	1.0	64.8	0.2	21.7	0.2	22.5	0.6	23.1	0.6
FeO*	5.36	0.13	7.8	0.3	5.03	0.05	6.3	0.3	6.0	0.2
MnO	0.187	0.003	0.074	0.001	0.192	0.002	0.20	0.01	0.19	0.01
MgO	21.9	0.5	26.1	0.5	21.02	0.12	21.3	0.3	21.0	0.3
CaO	5.7	0.3	0.03	0.06	4.49	0.07	6.17	0.17	6.7	0.3
Na_2O	0.02	0.02	0.34	0.18	0.07	0.05	nd		0.02	0.03
K_2O	0.003	0.003	0.02	0.02	0.01	0.01	0.01	0.01	0.001	0.001
P_2O_5	0.0074	0.0004	0.001	0.002	0.0021	0.0004	0.01	0.01	0.02	0.01
Total	100.00		100.00		100.00		100.00		100.00	
Sc (ppm)	340	40	5.0	0.6	230.3	1.5	271	14	249	11
V	83	10	128.9	1.8	67.1	1.2	104	7	96	7
Cr	1950	184	10230	60	2880	50	4400	300	3330	170
Co	25.6	0.7	80	5	22.8	0.3	40	8	36	2
Zn	23	6	640	15	28.9	0.8	37	8	36	8
Ga	37.0	1.5	587.4	9.8	39.7	0.7	45	5	45	3
Ge	80.9	0.9	24.4	0.2	99.7	1.9	90	14	83	4
D_{Sc}	5.9	0.7	0.058	0.008	5.24	0.10	5.7	0.5	7.1	0.7
D_{Ti}	0.27	0.03	0.084	0.008	0.272	0.012	0.246	0.015	0.26	0.02
D_V	1.8	0.2	2.75	0.19	1.57	0.03	1.93	0.19	2.1	0.3
D_{Cr}	9.7	1.3	54	11	10.3	0.3	8	2	13	3
D_{Mn}	1.22	0.05	0.46	0.03	1.333	0.015	1.22	0.10	1.19	0.13
D_{Fe}	0.65	0.03	0.95	0.06	0.708	0.009	0.66	0.04	0.59	0.04
D_{Co}	0.70	0.03	3.0	0.6	0.723	0.014	1.1	0.2	0.82	0.08
D_{Zn}	0.21	0.06	5.2	0.5	0.242	0.007	0.23	0.06	0.17	0.04
D_{Ga}	0.40	0.02	6.5	0.5	0.421	0.009	0.39	0.05	0.35	0.05
D_{Ge}	1.69	0.06	0.40	0.04	1.72	0.06	1.3	0.2	1.33	0.12

Table 13
Average mineral/melt partition coefficients for FRTE measured by LA-ICP-MS.

	ol/melt	s.d.	opx/melt	s.d.	cpx/melt	s.d.	grt/melt	s.d.	spl/melt	s.d.
D_{Sc}	0.150	0.003	0.495	0.011	0.84	0.04	5.98	0.11	0.058	0.008
D_{Ti}	0.0080	0.0007	0.0656	0.0018	0.124	0.006	0.262	0.004	0.084	0.008
D_V	0.140	0.003	1.06	0.03	1.48	0.04	1.84	0.04	2.75	0.19
D_{Cr}	0.79	0.06	8.8	0.5	7.5	0.6	10.2	0.4	54	11
D_{Mn}	0.781	0.014	0.640	0.012	0.768	0.018	1.241	0.017	0.46	0.03
D_{Fe}	1.034	0.016	0.546	0.010	0.488	0.010	0.654	0.007	0.95	0.06
D_{Co}	2.37	0.09	1.29	0.14	0.86	0.04	0.83	0.02	3.0	0.6
D_{Zn}	0.96	0.04	0.451	0.017	0.333	0.017	0.213	0.009	5.2	0.5
D_{Ga}	0.0260	0.0009	0.299	0.010	0.357	0.013	0.390	0.007	6.5	0.5
D_{Ge}	0.427[a]	0.010	0.87	0.02	0.87	0.03	1.51	0.03	0.40	0.04

[a] Experiment A842 was not included in the calculation of average D_{ge}^{ol} despite its equilibrium K_D^{Fe-Mg} because its s.d. ≈ value of the measurement.

demonstrate the influence of garnet over these ratios. We also calculate a near-solidus melt of spinel peridotite KLB-1 (Davis et al., 2009).

Additionally, we present a model of eclogite partial melting. This model also simulates modal batch melting at 3 GPa. FRTE partition coefficients for this model are from Pertermann et al. (2004) where available. For elements not measured in that study, eclogite-relevant partition coefficients are estimated taking into consideration compositional and temperature trends (see Appendix for model details and calculated compositions). Melt fractions and residual modes come from the 3 GPa partial melting experiments of Pertermann and Hirschmann (2003). Two source compositions are considered: average MORB (Arevalo and McDonough, 2010a) and altered oceanic crust (AOC) from the ODP site 801 "supersection" of Kelley et al. (2003). It is not clear how similar either of these compositions is to recycled lithologies present in the upper mantle. Considering

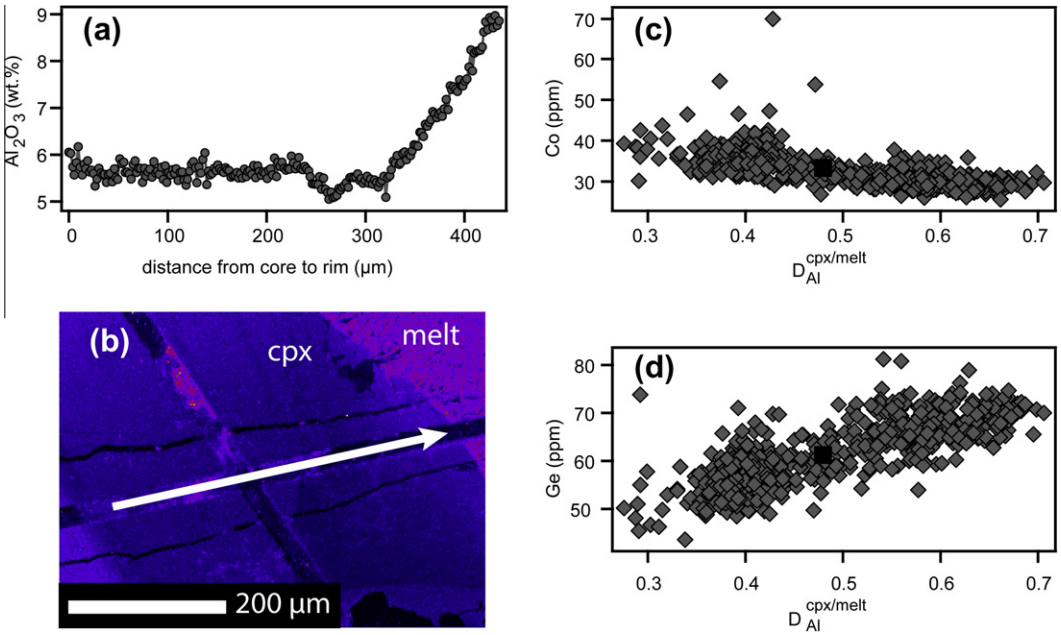

Fig. 2. Compositional zoning of cpx. (a) Al_2O_3 in A781 measured by LA-ICP-MS, scanning the laser along a linear path from crystal core to rim showing the increase in Al_2O_3 in the last 100 μm of the crystal rim. (b) False-color image showing a WDS map of Al_2O_3 concentration in the region of the laser track. The elevated Al_2O_3 concentration of the cpx rim is visible. (c and d) LA-ICP-MS measurements of Co and Ge along the laser track against $D_{Al}^{cpx/melt}$, which is simply the Al_2O_3 concentration measured in the cpx normalized to the Al_2O_3 content of the melt. The black square is the result of a linear regression to the value of $D_{Al}^{cpx/melt}$ obtained by Davis et al. (2011) for near-solidus partial melting of garnet lherzolite at 3 GPa.

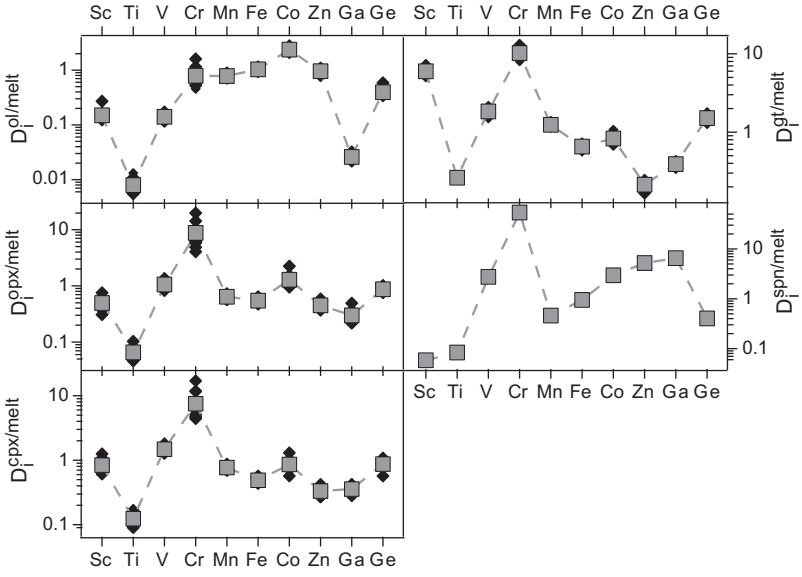

Fig. 3. Partition coefficients for FRTE measured by LA-ICP-MS. Black diamonds are mineral/melt partition coefficients from individual experiments. Gray squares are the average partition coefficients used in the peridotite partial melting model.

the extensive alteration possible owing to ~200 Ma of seafloor metamorphism, AOC seems like a more appropriate estimate than average MORB. Of course, neither takes into account compositional changes that may occur during subduction (Becker et al., 2000).

The models are compared to measurements of primitive OIB. OIB compositions were selected from those available in the GEOROC database (http://georoc.mpch-mainz.gwdg.de/georoc/, accessed 04/13/2011) by searching for data from island groups associated with small, predominantly alkaline hotspots. Island groups included were the Azores, the Canary Islands, the Cook and Austral Islands, the Marquesas, Pitcairn-Gambier, Samoa, the Society Islands, and St. Helena. In an effort to reduce the number

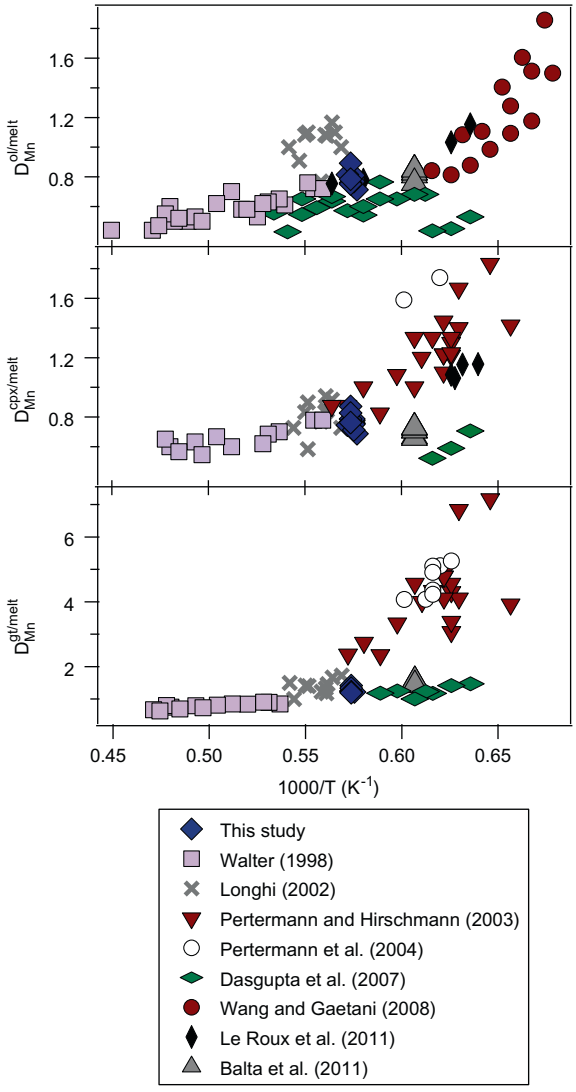

Fig. 4. Mn partitioning at different temperatures. Experiments included vary in pressure from 1 atm to 7 GPa, and come from peridotite-melt and eclogite-melt systems. It is notable that low-temperature melts of volatile-rich peridotites (Dasgupta et al., 2007; Balta et al., 2011) have lower $D_{Mn}^{cpx/melt}$ and $D_{Mn}^{grt/melt}$ than eclogite partial melts (Pertermann and Hirschmann, 2003; Pertermann et al., 2004) at similar temperatures. Zn and Co display similar behavior to Mn with temperature.

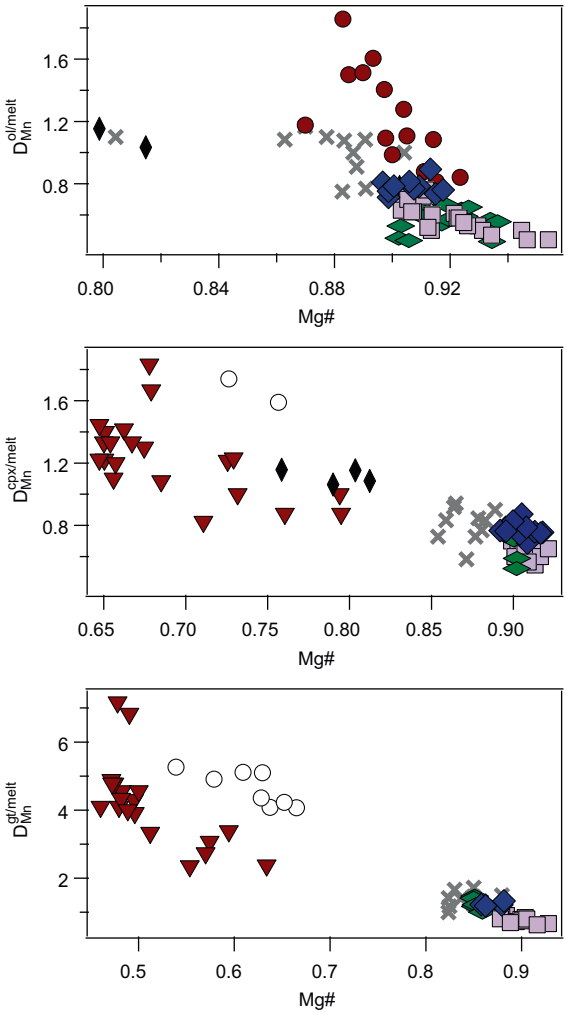

Fig. 5. Mn partitioning at different mineral Mg#. Symbols are as in Fig. 5. Mg# in each mineral phase is calculated as $(X_{Mg})/(X_{Mg}+X_{Fe})$.

of lavas with complex fractionation histories, lavas from these localities were included only if they had MgO >10 wt.% and less than <20 wt.%.

The focus of this discussion will be on a representative dataset of global OIB; however, there are flaws inherent in working with large database compilations. Some of the compositions we have accessed may have been modified by weathering and this may have affected FRTE abundances and ratios, including Fe/Mn (Huang et al., 2007). We are not aware of published detailed studies of how post-magmatic alteration affects the concentrations and ratios of FRTE in basaltic rocks, although Aiuppa et al. (2000) found that Fe was slightly less mobile than the other transition metals in groundwater that had leached Mt. Etna basalts. Geochemical indicators of alteration that may allow filtering of altered samples from the database include low K_2O/P_2O_5 (Frey et al., 1990), so we exclude those samples with $K_2O/P_2O_5 < 1.3$ (Frey et al., 1990; Huang et al., 2007). While this arbitrary cut-off substantially reduces the presence of altered OIB in the dataset, it is likely that some altered compositions remain. A detailed study of the effects of weathering on FRTE would improve estimates of the compositions of primitive OIB.

Another potential pitfall in employing large global databases for comparison to models of OIB genesis is that minor elements such as Mn are not always measured or reported precisely (Ruzicka et al., 2001; Humayun et al., 2004). To minimize this effect we include only measurements of Fe/Mn that report Mn (or MnO) concentrations to at least three significant digits. This method is less desirable than detailed regional studies using optimized analytical methods, but does help to refine the global dataset, reducing the range of OIB Fe/Mn ratios from 40–90 to

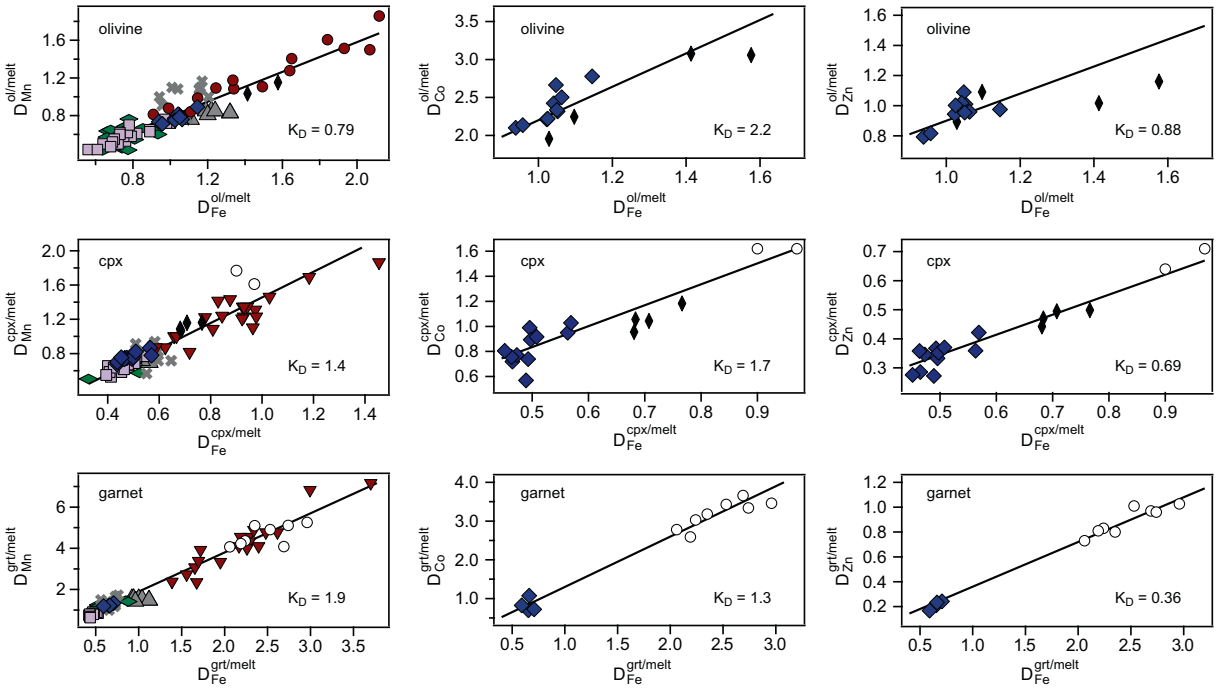

Fig. 6. Comparison of partitioning of Fe with other divalent FRTE. Symbols are as in Fig. 5. K_D is K_D^{i-j}, where i is the element on the y-axis and j is the element on the x-axis (see text for formulation of K_D^{i-j}). K_D is calculated by a linear regression forced through the origin. Opx is not shown, but values of K_D were calculated as: $K_D^{Mn-Fe} = 1.2$, $K_D^{Zn-Fe} = 0.84$, and $K_D^{Co-Fe} = 1.9$.

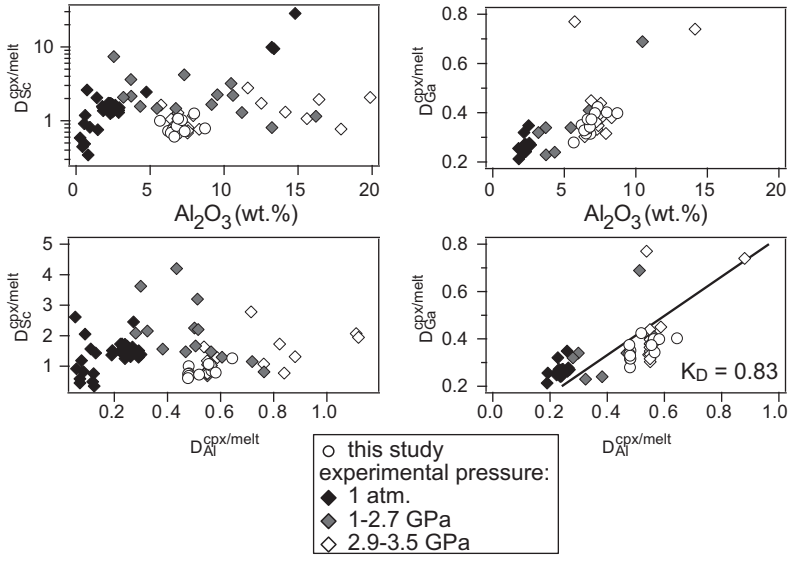

Fig. 7. Relationship between Sc and Ga partitioning in cpx and Al_2O_3 in cpx. Experimental data represented in this figure are from Ray et al. (1983), Hart and Dunn (1993), Hauri et al. (1994), Blundy et al. (1998), Hill et al. (2000), Pertermann and Hirschmann (2003), Pertermann et al. (2004), Adam and Green (2006), Mallmann and O'Neill (2009), and Hill et al. (2011). K_D calculated as in Fig. 6. Proportion of CaTs component determined following the pyroxene component calculations in Pertermann and Hirschmann (2002).

50–75. Because it is common for the same workers to analyze samples from a particular region, the filtering of low-precision Mn measurements eliminates some entire island groups from the Fe/Mn dataset. Lavas from the Canary Islands ($n = 28$), Cape Verde (115), and Samoa (1) are included in plots of Fe/Mn in Fig. 13.

4.3.1. Peridotite as the source of OIB

Among the FRTE ratios we have considered, Fe/Mn and Co/Fe are the most useful for identifying lava compositions that are inconsistent with derivation from partial melts of peridotite. As detailed above, bulk peridotite K_D^{Mn-Fe} is <1, thus Fe/Mn of a partial melt of peridotite

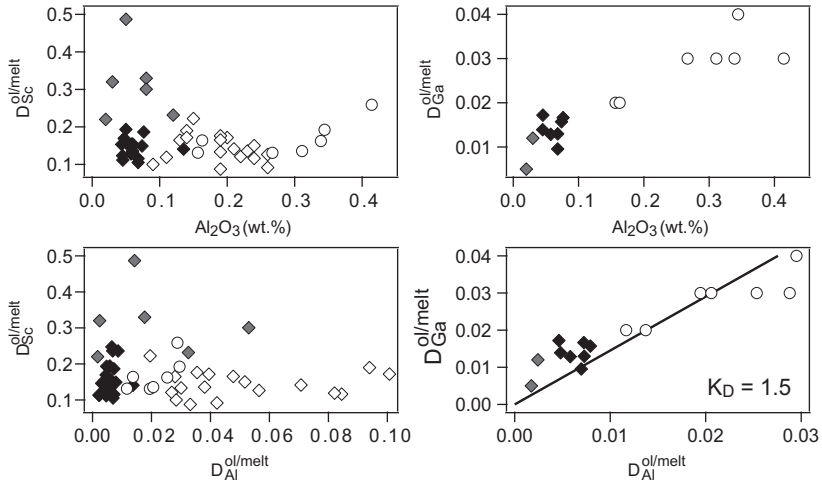

Fig. 8. Relationship between Sc and Ga partitioning in olivine and Al_2O_3 in olivine. Symbols as in Fig. 7. Experimental data represented in this figure are from Suzuki and Akaogi (1995), Taura et al. (1998), Adam and Green (2006), Evans et al. (2008), Mallmann and O'Neill (2009), and Grant and Wood (2010). K_D calculated as in Fig. 7.

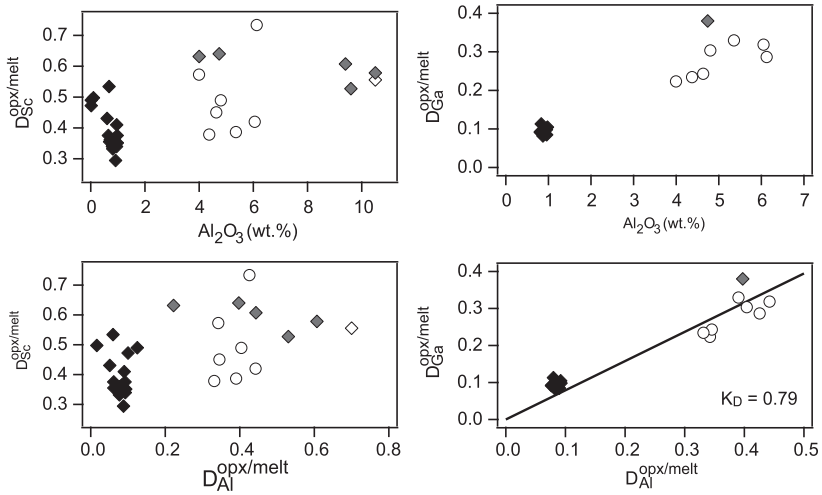

Fig. 9. Relationship between Sc and Ga partitioning in opx and Al_2O_3 in opx. Symbols as in Fig. 7. Experimental data represented in this figure are from Adam and Green (2006), Frei et al. (2009), Mallmann and O'Neill (2009), and van Kan Parker et al. (2010). K_D calculated as in Fig. 7.

cannot exceed that of its source. Most of the OIB considered in this study have Fe/Mn between 55 and 70 (Fig. 13). The three source compositions that we consider vary in Fe/Mn from 60 to 64. Lower Fe/Mn can be achieved at increased melt fractions, when residual garnet and cpx are diminished (Fig. 12), but OIB with Fe/Mn > 64 are not likely produced solely by partial melting of peridotite unless the source has an unusually high garnet mode or has a much higher Fe/Mn than the source compositions we have considered (Humayun et al., 2004). While garnet is increased in the mode of peridotites at pressures >3 GPa, the effect of increased garnet mode on melt Fe/Mn is likely counteracted by a reduced compatibility of Fe and Mn at higher pressures and temperatures of melting, as demonstrated by Humayun et al. (2004) using the experimental data of Walter (1998) and illustrated in Fig. 4.

Co/Fe may be the most effective ratio for discriminating between basalts that can or cannot be derived from a simple peridotitic source. Co is more compatible than Fe in all mantle minerals, so partial melts will have their lowest value of Co/Fe at low melt fractions. Only about 25% of OIB in the dataset (Fig. 13) have Co/Fe ratios higher than near-solidus melts of Ki5-8b (Lee, 2005) (Fig. 12); the rest seem to require an additional explanation or source.

Le Roux et al. (2010, 2011) argued that Zn/Fe too is an indicator of non-peridotitic lithologies, but using new data, we find it has less diagnostic potential than either Fe/Mn or Co/Fe. K_D^{Zn-Fe} between peridotite and melt is always <1, even at high melt fractions, so partial melts of peridotite will have a greater Zn/Fe content than their source. The highest Zn/Fe ratio that we model is for near-solidus melting of RP87-2 (Zangana et al., 1999) with (Zn/

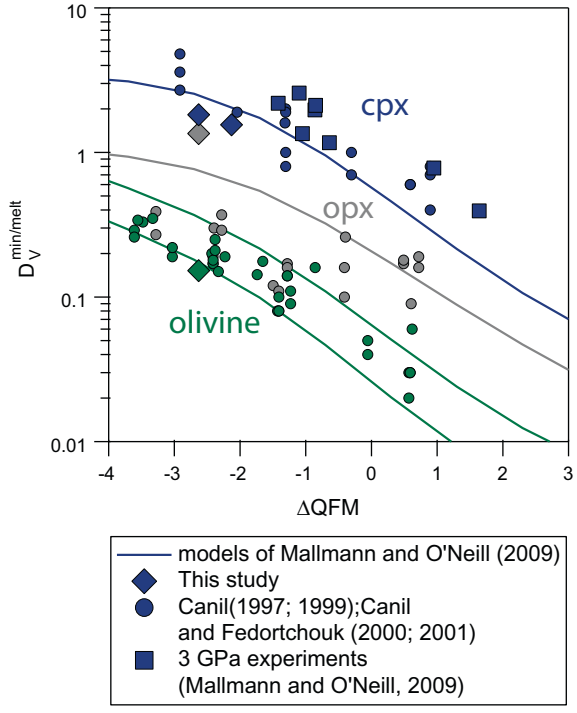

Fig. 10. Comparison of experimental values of D_V over a range of f_{O2}. ΔQFM values are log units of f_{O2} relative to the quartz–fayalite–magnetite buffer. For 100 kPa experiments, ΔQFM was calculated relative to O'Neill (1987). For experiments from this study and high-pressure experiments from Canil and Fedortchouk (2000); (Canil and Fedortchouk, 2001), the QFM buffer was calculated following Frost (1991) at the pressure and temperature of the experiment. ΔQFM for 3 GPa experiments from Mallmann and O'Neill (2009) are as reported by that study.

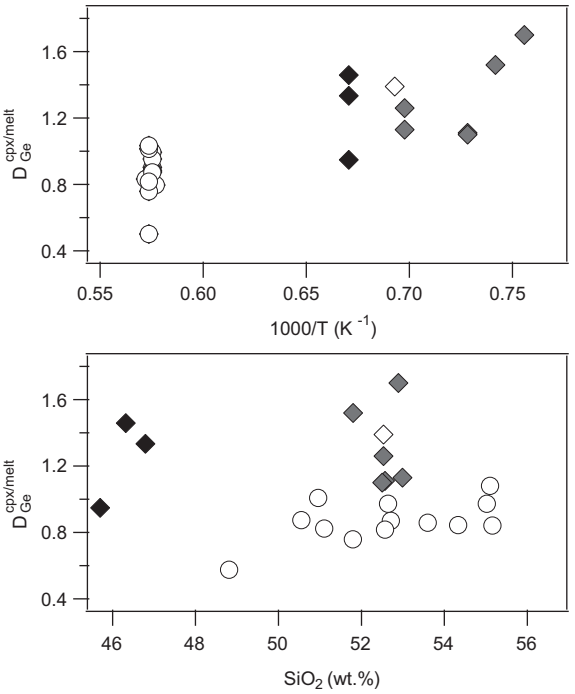

Fig. 11. Relationships of $D_{Ge}^{cpx/melt}$ to temperature and SiO_2 in cpx. Symbols are as in Fig. 7. Experimental data represented in this figure are from Hill et al. (2000) and Adam and Green (2006).

Fe) $* 10^4 = 13$; this maximum is sufficient to account for >75% of the Zn/Fe ratios in the OIB dataset (Fig. 13). Le Roux et al. (2011) found that fewer OIB fell within the range of Zn/Fe that they predicted for peridotite partial melting. While their determination of bulk peridotite K_D^{Zn-Fe} is similar to ours, they limited their source composition to PUM (McDonough and Sun, 1995). We argue that a range of potential source Zn/Fe ratios should be considered because source composition is the variable with the greatest leverage over Zn/Fe in partial melts (Fig. 12). RP87-2 falls on the high end of peridotite Zn/Fe found in the GEOROC database, but is not an outlier (see Appendix). Given current constraints on mantle compositional variability, Zn/Fe would be inconsistent with peridotitic source lithologies only in those OIB with (Zn/Fe) $* 10^4 > 13$. The generally lower Zn/Fe in MORB as compared to OIB is consistent with higher average degrees of partial melting, but may also be related to the presence of residual spinel. Zn is much more compatible in spinel than in any of the other peridotite minerals, and Zn/Fe is significantly lower in near-solidus melts that formed in the presence of a few percent of residual spinel than those from garnet peridotite (Fig. 12).

The ratio of Ga to Sc should also be helpful in characterizing source lithologies of oceanic basalts because Ga and Sc have similar compatibilities in olivine and pyroxenes, but are strongly fractionated by melting in the presence of garnet (Figs. 3 and 12). Primitive OIB vary in Ga/Sc from 0.4–1.1. The upper end of this range is slightly exceeded by near-solidus partial melting of garnet peridotite, irrespective of the starting composition chosen. The lower portion of the OIB global array is produced at a melt fraction of ~0.15, where garnet is exhausted from the residue and partial melts of peridotite have Ga/Sc. Thus, the entire range of OIB Ga/Sc can be accounted for by peridotite partial melting. Still, the Ga/Sc ratio places limits on the proportion of garnet in the source. For example, a source rock with a high modal abundance of garnet, either because it melts at high pressure or has been metasomatically enriched, could produce a magma with higher Fe/Mn and Zn/Fe, consistent with those OIB that fall outside the range of likely partial melts of peridotite, but such a source lithology would produce magmas with higher Ga/Sc than is seen in the global OIB dataset. A possible scenario that could lead to higher Fe/Mn and lower Co/Fe without affecting Ga/Sc is partial melting under oxidizing conditions; this possibility is considered in greater detail below.

Arevalo and McDonough (2010b) suggested that Ga/Ge may be an indicator of source lithology, based on the observation that Ga/Ge is higher in OIB than in MORB. We are unable to include Ga/Ge in Fig. 13 because Ge analyses in OIB are sparse (only one sample that passed the filter had been analyzed for Ge). Ga is more incompatible than Ge in all phases except spinel (Table 13, Fig. 3), and Ga/Ge is sensitive to melt fraction (Fig. 12). Ga/Ge is not sensitive

Table 14
Starting compositions used in the melting model.

	PUM[a]	Ki5–8b[b]	RP87–2[c]	AOC[d]	MORB[e]
Sc	16.2	15.5	19	37.4	36.8
Ti	1205	856	935	10200	8500
V	82	79.5	95	338	250
Cr	2625	–	3666	114	326
Mn	1045	1015	929	2014	1320
FeO*	8.06	8.11	7.62	12.33	9.36
Co	105	102	101	36.7	56
Zn	55	52.8	65	88.5	80
Ga	4	3.63	4.0	15.6	21
Ge	1.1	–	–	–	1.6
Mg#	89.3	–	89.8	47.3	59.9
Fe/Mn	59.9	62.08	63.7	47.6	55.1
$(Zn/Fe)*10^4$	8.8	8.38	11.0	9.2	11.0
$(Co/Fe)*10^4$	16.8	16.19	17.1	3.8	7.7
Ga/Sc	0.2	0.23	0.2	0.4	0.6
Ga/Ge	3.6	–	–	–	13.1
V/Sc	5.1	5.13	5.0	9.0	6.8

[a] McDonough and Sun (1995).
[b] Lee (2005).
[c] Zangana et al. (1999).
[d] Kelley et al. (2003).
[e] Arevalo and McDonough (2010a).

to the presence or absence of residual garnet (Fig. 12), but is affected by even small amounts of spinel. Lower Ga/Ge in MORB compared to OIB is likely owing to the larger average melt fraction of the former, but may also be a result of residual spinel in the MORB source.

Fe-enrichment of the source peridotite could lead to high Fe/Mn in some OIB, perhaps by interaction of core material with the sources of mantle plumes (Humayun et al., 2004). Le Roux et al. (2011) argued that incorporation of core material would also lead to decreased Zn/Fe and increased Co/Fe in the source peridotite (McDonough, 2003). If OIB sources have been affected by interaction with core, the consequences for FRTE geochemistry depend on the details of interaction, which could range from bulk addition of core (Brandon and Walker, 2005; Sobolev et al., 2005), to exsolution of an FeO-rich melt (Humayun et al., 2004), to diffusive exchange (Hayden and Watson, 2007). Adjusting the PUM composition by adding 2.5 wt.% of core material with the composition from McDonough (2003) leads to a near-solidus melt with $Fe/Mn = 73$, $(Zn/Fe)*10^4 = 8$, and $(Co/Fe)*10^4 = 9$. Neither this combination of ratios nor the compositional trajectory it implies corresponds to primitive OIB compositions (Fig. 13). Thus, FRTE ratios in OIB are not consistent with models of metal addition to the sources of mantle plumes, though they do not conclusively exclude other possible interactions, given the extreme conditions under which they might occur.

Because the compatibilities of V and Fe are sensitive to f_{O2}, element ratios that include V or Fe will be sensitive to differences in source f_{O2}. Estimates of Fe oxidation state in OIB lavas vary considerably. Observed $Fe^{3+}/\Sigma Fe$ ranges from 0.06–0.14 in Hawaii (Rhodes and Vollinger, 2005) to 0.17–0.25 in the Canary Islands (Gurenko and Schmincke, 2000). $Fe^{3+}/\Sigma Fe$ in MORB varies between 0.13–0.17 (Cottrell and Kelley, 2011), so individual OIB suites may come from either more or less oxidizing source regions than the MORB-source, although OIB appear on average to be more oxidized than MORB (Mallmann and O'Neill, 2007). Our experiments are more reduced than any of these ranges (QFM-2 to QFM-3 and therefore $Fe^{3+}/\Sigma Fe = 0.04$–0.06, Kress and Carmichael, 1991), so model melt compositions will tend to underestimate Fe/Mn and overestimate Zn/Fe and Co/Fe compared to melts formed under the same redox conditions as primary OIB. For example, if we recalculate model partial melts of peridotite with the composition of RP87-2 (Zangana et al., 1999) and assume a source Fe_2O_3 content of 0.3 wt.% (Canil et al., 1994) and $D_{Fe3+} = 0.1$, then the near-solidus melt will have $Fe/Mn = 77.5$, $(Zn/Fe)*10^4 = 10.3$, and $(Co/Fe)*10^4 = 6.3$. These are Fe/Mn and Co/Fe ratios that cannot be achieved by partial melting of peridotite under more reducing conditions and suggest that some of the variation in OIB FRTE ratios could be caused by differences in the f_{O2} of their source regions. Further study of the partitioning behavior of Fe^{3+} and f_{O2} in OIB source regions are required to better evaluate the role of Fe oxidation state in influencing these ratios.

Ratios in basalts of V or Fe to other FRTE that do not exhibit more than one valence state may record the f_{O2} in the source region; for example, Ti/V (Shervais, 1982), V/Sc (Li and Lee, 2004; Lee et al., 2005), and Zn/Fe (Lee et al., 2010) in basalts and peridotites are potential indicators of f_{O2} in basalt source regions. Fig. 13 demonstrates that most primitive OIB have higher V/Sc than any melts we have modeled, consistent with our expectation that f_{O2} is greater in OIB source regions than in our experiments. Lee et al. (2005) note that intraplate basalts show a greater range of V/Sc than do MORB and suggest this may be related to more oxidizing conditions, lower melt fractions, or the presence of garnet in the melting residue. Our model confirms that V/Sc is highly sensitive to residual garnet, the presence or absence of which may change V/Sc in the coexisting melt by a factor of 2 (Fig. 12). Thus, it is likely that some of the variation of V/Sc in the global OIB dataset is due to the differences in modal proportion of residual garnet, rather than variation in source f_{O2}.

When considered individually, many FRTE ratios in OIB appear to be consistent with derivation from a peridotite source, but when several FRTE ratios are considered simultaneously, few OIB have compositions that resemble partial melts of peridotite. This is clearly demonstrated in Fig. 13, which shows, for example, that many OIB have Zn/Fe ratios similar to partial melts of peridotite but Fe/Mn ratios too high to have come from a peridotite source. Few OIB have Co/Fe ratios large enough to be consistent with partial melting of peridotite, and among those few many also have greater Fe/Mn or Zn/Fe than partial melts of peridotite. However, it is possible that partial melts of peridotite formed under more oxidizing conditions may resemble primitive OIB more closely in Fe/Mn and Co/Fe. If f_{O2} cannot account for all these variations, then it seems that many OIB have been at least partly derived from some other melting lithology.

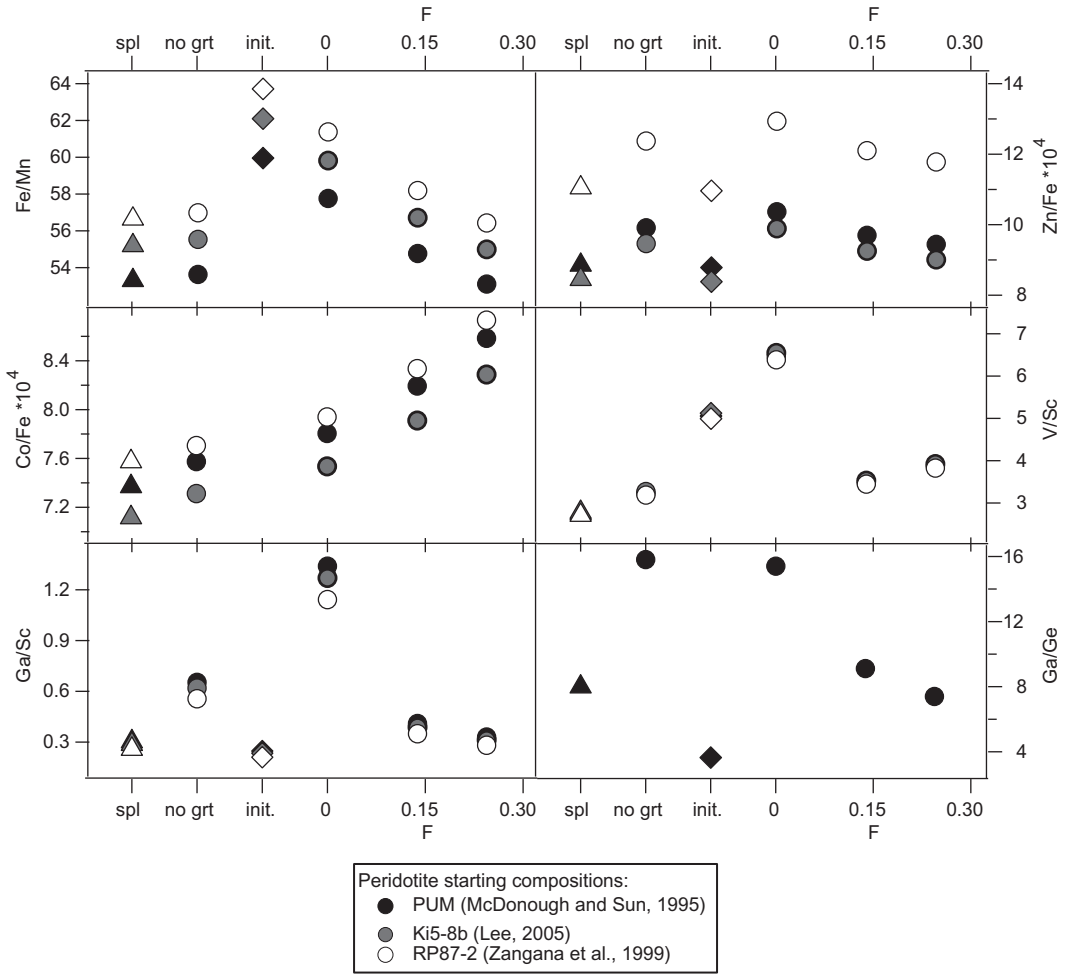

Fig. 12. Results of the peridotite partial melting model. Numbers on the right side of the *x*-axis indicate melt fractions. Diamonds above the tick marked "init." are the ratios of the source peridotite. Circles above the tick labeled "no grt" are model melts at a melt fraction of 0 with the same relative proportions of olivine, opx, and cpx as the $F = 0$ partial melts of garnet peridotite, but with garnet absent from the residue. The triangles above the tick labeled "spl" are model near-solidus melts of a spinel peridotite with the same mineral mode as KLB-1 (Davis et al., 2009). The initial ratios of Co/Fe are much higher than in model melts and are not depicted but are available in Table 14.

4.3.2. Partial melts of eclogite and magma mixing

Partial melting of recycled oceanic crust is widely considered to contribute in part to the genesis of OIB based on major element chemistry (Hauri, 1996; Kogiso et al., 1998, 2003), trace element ratios (Hofmann and White, 1982; Weaver, 1991; Chauvel et al., 1992), and isotopic ratios (Hofmann and White, 1982; Christensen and Hofmann, 1994). We consider a model of partial melting of MORB-like eclogite to determine whether these melts have FRTE ratios that are a better fit for OIB than partial melts of peridotite. Partition coefficients for many FRTE relevant to partial melting of eclogite are provided by a trace element partitioning study in the eclogite + melt system by Pertermann et al. (2004). These partition coefficients form the basis of the eclogite partial melting model; the details of model are described in the Appendix.

The results of the eclogite partial melting model are presented along with model partial melts of peridotite and OIB compositions in Fig. 13. In each part of Fig. 13, the lowest melt fraction partial melts of eclogite plot furthest from the partial melts of peridotite. For most of the ratios considered, the MORB and AOC compositions plot over top of each other with the AOC melts plotting at less extreme compositions for a given melt fraction. The only significant exception is that partial melts of the AOC composition have much lower Co/Fe than do the MORB compositions. AOC has both higher Fe and lower Co concentrations than does average MORB. Fe/Mn, Zn/Fe, Ga/Sc, and Ga/Ge (not shown) all decrease with increasing melt fraction. V/Sc and Co/Fe are relatively insensitive to melt fraction except that Co/Fe increases significantly in the melt once garnet is exhausted from the residue (the highest melt fraction point).

Low-degree partial melts of eclogite do not resemble OIB in any of these ratios. As melt fraction increases, partial melts of eclogite move along compositional trajectories toward partial melts of peridotite. At extremely high melt fractions, when cpx is the only residual phase, FRTE ratios of partial melts of eclogite become indistinguishable from near-solidus partial melts of peridotite (with the notable

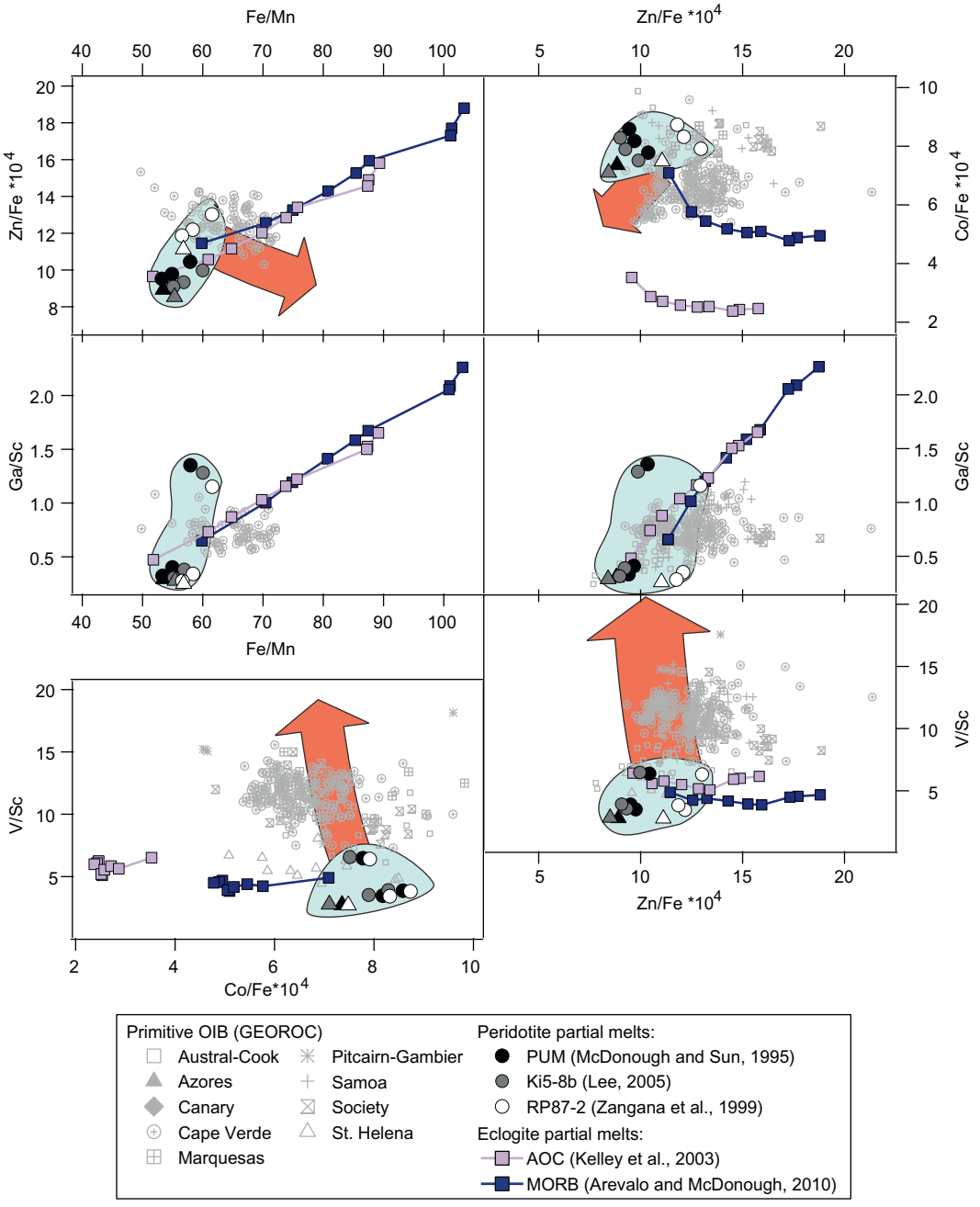

Fig. 13. Results of the peridotite and eclogite partial melting models plotted with primitive OIB. Primitive OIB have MgO > 10% and <20%. Localities and other selection criteria are given in the text. As in Fig. 12, the triangles denote near-solidus melts of spinel peridotite. The blue field drawn around the partial melts of peridotite is meant to highlight the likely range of peridotite partial melting at 3 GPa. The eclogite-derived melts located furthest from the peridotite partial melting field are those with the lowest melt fraction. Red arrows indicate inferred effect of increased f_{O2} during partial melting. General trends for these arrows were determined by assuming bulk peridotite $D_{Fe3+} = 0.1$ and increasing the amount of Fe_2O_3 in starting peridotite. Changes in mineral/melt D_V with f_{O2} follow the model of (Mallmann and O'Neill, 2009).

exception of Co/Fe in partial melts of the AOC starting composition). The choice of starting compositions is critical to estimates of the minimum melt fraction required for a pyroxenite partial melt to fall into the field of OIB compositions. For the MORB starting composition, partial melts have FRTE ratios more extreme than any primitive OIB at melt fractions <0.60 (~1475 °C at 3 GPa). If the AOC starting composition is considered, then lower-degree melts appear to be plausible primary OIB magmas, except that even the lowest Co/Fe ratios in primitive OIB are a factor of two higher than the most Co-rich partial melts of AOC.

Few primitive OIB appear to be consistent with derivation solely from fertile garnet peridotite, and few if any are

consistent with derivation solely from eclogitic partial melting, so we must consider the possibility that OIB result from magma mixing. First, let us consider partial melting of peridotite and eclogite under similar conditions beneath oceanic lithosphere (~100 km depth, $P \approx 3$ GPa). The solidus of garnet peridotite at these pressures is ~1450 °C (Davis et al., 2011). MORB-like eclogite will have reached a melt fraction >0.50 at this temperature (Pertermann and Hirschmann, 2003). This suggests that magma mixing is most likely to occur between low-degree partial melts of peridotite and high-degree partial melts of eclogite. We have not included mixing curves in Fig. 13 to avoid clutter, but a casual examination of these compositional graphs reveals compositional groups of OIB that are not easily reconciled by this kind of magma mixing scenario. In Zn/Fe–Fe/Mn space, mixing curves will be convex up, suggesting that OIB with high Fe/Mn and low Zn/Fe do not result from mixing peridotitic and eclogitic partial melts. Such melts are compatible with the hypothesis that the melting source region is enriched in Fe relative to the rest of the upper mantle (Humayun et al., 2004; Qin and Humayun, 2008). In Ga/Sc–Fe/Mn and Ga/Sc–Zn/Fe space, mixing curves will be convex down. Any addition of eclogitic partial melts to account for high Fe/Mn or Zn/Fe is accompanied by excessive increases in Ga/Sc of the resulting mixed magma. This can be remedied if we allow mixing of high-degree partial melts of peridotite with near-solidus melts of eclogite, but these magmas will not be stable at the same temperatures and pressures.

We have not considered the possibility that near-solidus partial melts of eclogite react with peridotite below its solidus to form pyroxenite, which may then produce magmas with characteristics intermediate to partial melts of peridotite and eclogite (e.g., Yaxley and Green, 1998; Sobolev et al., 2005, 2007). This process is too complex to address in this study, although perhaps from the point of view of trace elements, mixing between low-degree melts of both sources could be considered a close approximation. It may be that partial melting of reaction pyroxenite is broadly compatible with FRTE compositions of primitive OIB, but we urge caution in attempting to quantify precise contributions of such lithologies to particular magmatic suites. Any model attempting to do so must make assumptions about the degrees of melting of the eclogite, the resulting reaction pyroxenite, and the peridotite end-member, as well as starting compositions and residual modes for each of these lithologies. We have shown that each of these variables is of critical importance to the resulting melt compositions, even when limited by the restricted compositional range we have considered.

5. CONCLUSIONS

Experimentally determined partition coefficients for near-solidus partial melting of garnet peridotite at 3 GPa confirm that high modal proportions of cpx and garnet in a peridotite melting source tend to drive melts to higher Fe/Mn, while residual olivine tends to counteract this effect. Residual cpx and garnet are more efficient at fractionating Zn and Fe than is olivine, although Zn is less compatible than Fe in all peridotite mineral phases. Trivalent cations like Sc^{3+} and Ga^{3+} are also strongly fractionated by residual garnet and spinel, but not by other mantle phases. These partition coefficients were used to model partial melting of peridotite at 3 GPa for comparison with primitive OIB. While model partial melts of peridotite are similar to many OIB when key FRTE ratios are considered individually, few OIB resemble partial melts of peridotite when multiple ratios are considered simultaneously. There remains an important caveat that some of these ratios in natural basalts may have been affected by weathering, and the effects of post-magmatic alteration on FRTE ratios are poorly constrained. A clear result of the model is that FRTE ratios in peridotite-derived melts are sensitive to modal mineralogy, melt fraction, and source composition. The model supports the interpretation that many OIB have greater Fe/Mn than can be achieved by melting of fertile garnet peridotite, at least under relatively reducing conditions. Partial melts of peridotite are also expected to have greater Co/Fe than most primitive OIB. Some OIB have higher Zn/Fe than can be reconciled with partial melting of peridotite, although this ratio is not nearly as effective as Fe/Mn or Co/Fe at identifying basalts from non-peridotitic sources. We add to these petrogenetic indicators Ga/Sc, which is highly sensitive to the presence of garnet in the residue. Nearly all OIB have Ga/Sc consistent with derivation from garnet peridotite.

Fe/Mn, Zn/Fe, and Co/Fe are sensitive to the choice of peridotite source composition. We have considered three different fertile peridotite compositions in our melting model, but these may not completely describe the range of potential peridotite melting sources available in the upper mantle. It is difficult to evaluate how well these three compositions represent global peridotite variation because many of the FRTE and Ga and Ge are often overlooked in trace element studies of peridotites and basalts. While we cannot determine precisely the effect of melting under conditions more oxidizing than our experiments, partial melts of peridotite generated at greater f_{O2} should lead to higher Fe/Mn and lower Co/Fe and Zn/Fe, more similar to some OIB.

Mixing of partial melts of peridotite with melts from recycled lithologies is broadly consistent with FRTE systematics of OIB; however this is largely dependent on the assumed composition of recycled oceanic crust. For example, if mantle eclogites have FRTE compositions similar to altered oceanic crust, then it may be difficult to reconcile the melts they produce with the much higher Co/Fe ratios of OIB. Partial melting of reaction pyroxenites may be involved in the production of OIB, but we urge caution when applying models to quantify their contributions to OIB genesis. Such models are dependent on poorly-constrained assumptions about compositions, modal mineralogy, and melt fractions of recycled oceanic crustal lithologies. Finally, models of core–mantle interaction that assume physical entrainment of metal into OIB sources fail to predict the magnitude or the direction of the observed trends in Co/Fe ratios.

ACKNOWLEDGEMENTS

This paper was improved after thoughtful reviews from Veronique Le Roux and Dante Canil. This work was supported by a grant from NSF (EAR1019744).

APPENDIX A. SUPPLEMENTARY DATA

Supplementary data associated with this article can be found, in the online version, at http://dx.doi.org/10.1016/j.gca.2012.11.009.

REFERENCES

Adam J. and Green T. (2006) Trace element partitioning between mica- and amphibole-bearing garnet lherzolite and hydrous basanitic melt: 1. Experimental results and the investigation of controls on partitioning behaviour. *Contrib. Miner. Petrol.* **152**, 1–17.

Aiuppa A., Allard P., D'Alessandro W., Michel A., Parello F., Treuil M. and Valenza M. (2000) Mobility and fluxes of major, minor and trace metals during basalt weathering and groundwater transport at Mt. Etna volcano (Sicily). *Geochim. Cosmochim. Acta* **64**, 1827–1841.

Arevalo R. and McDonough W. F. (2010a) Chemical variations and regional diversity observed in MORB. *Chem. Geol.* **271**, 70–85.

Arevalo R. and McDonough W. F. (2010b) Gallium and germanium abundances in MORB and OIB: evidence for pyroxenitic source components? *Geochim. Cosmochim. Acta* **74**, A32.

Balta J. B., Asimow P. D. and Mosenfelder J. L. (2011) Hydrous, low-carbon melting of garnet peridotite. *J. Petrol.* **52**, 2079–2105.

Beattie P., Ford C. and Russell D. (1991) Partition-coefficients for olivine-melt and ortho-pyroxene-melt systems. *Contrib. Miner. Petrol.* **109**, 212–224.

Becker H., Jochum K. P. and Carlson R. W. (2000) Trace element fractionation during dehydration of eclogites from high-pressure terranes and the implications for element fluxes in subduction zones. *Chem. Geol.* **163**, 65–99.

Blundy J. and Wood B. (2003) Partitioning of trace elements between crystals and melts. *Earth Planet. Sci. Lett.* **210**, 383–397.

Blundy J. D., Robinson J. A. C. and Wood B. J. (1998) Heavy REE are compatible in clinopyroxene on the spinel lherzolite solidus. *Earth Planet. Sci. Lett.* **160**, 493–504.

Brandon A. D. and Walker R. J. (2005) The debate over core–mantle interaction. *Earth Planet. Sci. Lett.* **232**, 211–225.

Canil D. (1997) Vanadium partitioning and the oxidation state of Archaean komatiite magmas. *Nature* **389**, 842–845.

Canil D. (1999) Vanadium partitioning between orthopyroxene, spinel and silicate melt and the redox states of mantle source regions for primary magmas. *Geochim. Cosmochim. Acta* **63**, 557–572.

Canil D. and Fedortchouk Y. (2000) Clinopyroxene–liquid partitioning for vanadium and the oxygen fugacity during formation of cratonic and oceanic mantle lithosphere. *J. Geophys. Res. Solid Earth* **105**, 26003–26016.

Canil D. and Fedortchouk Y. (2001) Olivine–liquid partitioning of vanadium and other trace elements, with applications to modern and ancient picrites. *Can. Mineral.* **39**, 319–330.

Canil D., O'Neill H. S. C., Pearson D. G., Rudnick R. L., McDonough W. F. and Carswell D. A. (1994) Ferric iron in peridotites and mantle oxidation states. *Earth Planet. Sci. Lett.* **123**, 205–220.

Chase C. G. (1981) Oceanic island Pb – 2-stage histories and mantle evolution. *Earth Planet. Sci. Lett.* **52**, 277–284.

Chauvel C., Hofmann A. W. and Vidal P. (1992) HIMU – EM: the French-Polynesian connection. *Earth Planet. Sci. Lett.* **110**, 99–119.

Christensen U. R. and Hofmann A. W. (1994) Segregation of subducted oceanic-crust in the convecting mantle. *J. Geophys. Res. Solid Earth* **99**, 19867–19884.

Cottrell E. and Kelley K. A. (2011) The oxidation state of Fe in MORB glasses and the oxygen fugacity of the upper mantle. *Earth Planet. Sci. Lett.* **305**, 270–282.

Dasgupta R., Hirschmann M. M. and Smith N. D. (2007) Partial melting experiments of peridotite + CO_2 at 3 GPa and genesis of alkalic ocean island basalts. *J. Petrol.* **48**, 2093–2124.

Davis F. A., Hirschmann M. M. and Humayun M. (2011) The composition of the incipient partial melt of garnet peridotite at 3 GPa and the origin of OIB. *Earth Planet. Sci. Lett.* **308**, 380–390.

Davis F. A., Tangeman J. A., Tenner T. J. and Hirschmann M. M. (2009) The composition of KLB-1 peridotite. *Am. Mineral.* **94**, 176–180.

Evans T. M., O'Neill H. S. C. and Tuff J. (2008) The influence of melt composition on the partitioning of REEs, Y, Sc, Zr and Al between forsterite and melt in the system CMAS. *Geochim. Cosmochim. Acta* **72**, 5708–5721.

Fellows S. A. and Canil D. (2012) Experimental study of the partitioning of Cu during partial melting of Earth's mantle. *Earth Planet. Sci. Lett.* **337–338**, 133–143.

Frei D., Liebscher A., Franz G., Wunder B., Klemme S. and Blundy J. (2009) Trace element partitioning between orthopyroxene and anhydrous silicate melt on the lherzolite solidus from 1.1 to 3.2 GPa and 1230 to 1535 °C in the model system Na_2O–CaO–MgO–Al_2O_3–SiO_2. *Contrib. Miner. Petrol.* **157**, 473–490.

Frey F. A., Wise W. S., Garcia M. O., West H., Kwon S. T. and Kennedy A. (1990) Evolution of Mauna-Kea volcano, Hawaii – petrologic and geochemical constraints on postshield volcanism. *J. Geophys. Res. Solid Earth Planets* **95**, 1271–1300.

Frost B. R. (1991) Introduction to oxygen fugacity and its petrologic significance. *Rev. Mineral.* **25**, 1–9.

Frost D. J. and Wood B. J. (1997) Experimental measurements of the fugacity of CO_2 and graphite/diamond stability from 35 to 77 kbar at 925 to 1650 °C. *Geochim. Cosmochim. Acta* **61**, 1565–1574.

Gaboardi M. and Humayun M. (2009) Elemental fractionation during LA-ICP-MS analysis of silicate glasses: implications for matrix-independent standardization. *J. Anal. At. Spectrom.* **24**, 1188–1197.

Govindaraju K. (1994) 1994 compilation of working values and sample description for 383 geostandards. *Geostand. Newslett.* **18**, 1–42.

Grant K. J. and Wood B. J. (2010) Experimental study of the incorporation of Li, Sc, Al and other trace elements into olivine. *Geochim. Cosmochim. Acta* **74**, 2412–2428.

Gurenko A. A. and Schmincke H. U. (2000) S concentrations and its speciation in Miocene basaltic magmas north and south of Gran Canaria (Canary Islands): constraints from glass inclusions in olivine and clinopyroxene. *Geochim. Cosmochim. Acta* **64**, 2321–2337.

Hart S. R. and Dunn T. (1993) Experimental cpx melt partitioning of 24 trace-elements. *Contrib. Miner. Petrol.* **113**, 1–8.

Hauri E. H. (1996) Major-element variability in the Hawaiian mantle plume. *Nature* **382**, 415–419.

Hauri E. H., Wagner T. P. and Grove T. L. (1994) Experimental and natural partitioning of Th, U, Pb and other trace-elements between garnet, clinopyroxene and basaltic melts. *Chem. Geol.* **117**, 149–166.

Hayden L. A. and Watson E. B. (2007) A diffusion mechanism for core–mantle interaction. *Nature* **450**, 709–711.

Herzberg C., Gasparik T. and Sawamoto H. (1990) Origin of mantle peridotite – constraints from melting experiments to 16.5 GPa. *J. Geophys. Res. Solid Earth Planets* **95**, 15779–15803.

Hill E., Blundy J. D. and Wood B. J. (2011) Clinopyroxene-melt trace element partitioning and the development of a predictive model for HFSE and Sc. *Contrib. Miner. Petrol.* **161**, 423–438.

Hill E., Wood B. J. and Blundy J. D. (2000) The effect of Ca-Tschermaks component on trace element partitioning between clinopyroxene and silicate melt. *Lithos* **53**, 203–215.

Hirose K. (1997) Partial melt compositions of carbonated peridotite at 3 GPa and role of CO_2 in alkali-basalt magma generation. *Geophys. Res. Lett.* **24**, 2837–2840.

Hirschmann M. M. and Stolper E. M. (1996) A possible role for garnet pyroxenite in the origin of the ''garnet signature'' in MORB. *Contrib. Miner. Petrol.* **124**, 185–208.

Hofmann A. W. and White W. M. (1982) Mantle plumes from ancient oceanic-crust. *Earth Planet. Sci. Lett.* **57**, 421–436.

Huang S. C., Humayun M. and Frey F. A. (2007) Iron/manganese ratio and manganese content in shield lavas from Ko'olau Volcano, Hawai'i. *Geochim. Cosmochim. Acta* **71**, 4557–4569.

Humayun M., Davis F. A. and Hirschmann M. M. (2010) Major element analysis of natural silicates by laser ablation ICP-MS. *J. Anal. At. Spectrom.* **25**, 998–1005.

Humayun M., Qin L. P. and Norman M. D. (2004) Geochemical evidence for excess iron in the mantle beneath Hawaii. *Science* **306**, 91–94.

Humayun M., Simon S. B. and Grossman L. (2007) Tungsten and hafnium distribution in calcium–aluminum inclusions (CAIs) from Allende and Efremovka. *Geochim. Cosmochim. Acta* **71**, 4609–4627.

Jackson M. G. and Dasgupta R. (2008) Compositions of HIMU, EM1, and EM2 from global trends between radiogenic isotopes and major elements in ocean island basalts. *Earth Planet. Sci. Lett.* **276**, 175–186.

Jochum K. P., Stoll B., Herwig K., Willbold M., Hofmann A. W., Amini M., Aarburg S., Abouchami W., Hellebrand E., Mocek B., Raczek I., Stracke A., Alard O., Bouman C., Becker S., Ducking M., Bratz H., Klemd R., de Bruin D., Canil D., Cornell D., de Hoog C. J., Dalpe C., Danyushevsky L., Eisenhauer A., Gao Y. J., Snow J. E., Goschopf N., Gunther D., Latkoczy C., Guillong M., Hauri E. H., Hofer H. E., Lahaye Y., Horz K., Jacob D. E., Kassemann S. A., Kent A. J. R., Ludwig T., Zack T., Mason P. R. D., Meixner A., Rosner M., Misawa K. J., Nash B. P., Pfander J., Premo W. R., Sun W. D., Tiepolo M., Vannucci R., Vennemann T., Wayne D. and Woodhead J. D. (2006) MPI-DING reference glasses for in situ microanalysis: new reference values for element concentrations and isotope ratios. *Geochem. Geophys. Geosyst.* **7**.

Jochum K. P., Weis U., Stoll B., Kuzmin D., Yang Q. C., Raczek I., Jacob D. E., Stracke A., Birbaum K., Frick D. A., Gunther D. and Enzweiler J. (2011) Determination of reference values for NIST SRM 610–617 glasses following ISO guidelines. *Geostand. Geoanal. Res.* **35**, 397–429.

Johnson K. T. M. (1998) Experimental determination of partition coefficients for rare earth and high-field-strength elements between clinopyroxene, garnet, and basaltic melt at high pressures. *Contrib. Miner. Petrol.* **133**, 60–68.

Kelley K. A., Plank T., Ludden J. and Staudigel H. (2003) Composition of altered oceanic crust at ODP Sites 801 and 1149. *Geochem. Geophys. Geosyst.* **4**.

Kogiso T., Tatsumi Y., Shimoda G. and Barsczus H. G. (1997) High μ (HIMU) ocean island basalts in southern Polynesia: new evidence for whole mantle scale recycling of subducted oceanic crust. *J. Geophys. Res. Solid Earth* **102**, 8085–8103.

Kogiso T., Hirose K. and Takahashi E. (1998) Melting experiments on homogeneous mixtures of peridotite and basalt: application to the genesis of ocean island basalts. *Earth Planet. Sci. Lett.* **162**, 45–61.

Kogiso T., Hirschmann M. M. and Frost D. J. (2003) High-pressure partial melting of garnet pyroxenite: possible mafic lithologies in the source of ocean island basalts. *Earth Planet. Sci. Lett.* **216**, 603–617.

Krawczynski M. J. and Grove T. L. (2012) Experimental investigation of the influence of oxygen fugacity on the source depths for high titanium lunar ultramafic magmas. *Geochim. Cosmochim. Acta* **79**, 1–19.

Kress V. C. and Carmichael I. S. E. (1991) The compressibility of silicate liquids containing Fe_2O_3 and the effect of composition, temperature, oxygen fugacity and pressure on their redox states. *Contrib. Miner. Petrol.* **108**, 82–92.

Le Roux V., Lee C. T. A. and Turner S. J. (2010) Zn/Fe systematics in mafic and ultramafic systems: implications for detecting major element heterogeneities in the Earth's mantle. *Geochim. Cosmochim. Acta* **74**, 2779–2796.

Le Roux V., Dasgupta R. and Lee C. T. A. (2011) Mineralogical heterogeneities in the Earth's mantle: constraints from Mn, Co, Ni and Zn partitioning during partial melting. *Earth Planet. Sci. Lett.* **307**, 395–408.

Lee C. T. A. (2005) Trace element evidence for hydrous metasomatism at the base of the North American lithosphere and possible association with Laramide low-angle subduction. *J. Geol.* **113**, 673–685.

Lee C. T. A., Leeman W. P., Canil D. and Li Z. X. A. (2005) Similar V/Sc systematics in MORB and arc basalts: implications for the oxygen fugacities of their mantle source regions. *J. Petrol.* **46**, 2313–2336.

Lee C. T. A., Luffi P., Le Roux V., Dasgupta R., Albarede F. and Leeman W. P. (2010) The redox state of arc mantle using Zn/Fe systematics. *Nature* **468**, 681–685.

Li Z. X. A. and Lee C. T. A. (2004) The constancy of upper mantle f_{O2} through time inferred from V/Sc ratios in basalts. *Earth Planet. Sci. Lett.* **228**, 483–493.

Mallmann G. and O'Neill H. S. C. (2007) The effect of oxygen fugacity on the partitioning of Re between crystals and silicate melt during mantle melting. *Geochim. Cosmochim. Acta* **71**, 2837–2857.

Mallmann G. and O'Neill H. S. C. (2009) The crystal/melt partitioning of V during mantle melting as a function of oxygen fugacity compared with some other elements (Al, P, Ca, Sc, Ti, Cr, Fe, Ga, Y, Zr and Nb). *J. Petrol.* **50**, 1765–1794.

Matzen A. K., Baker M. B., Beckett J. R. and Stolper E. M. (2009) The temperature and pressure dependence of Ni partitioning between olivine and MgO-rich silicate melt. *Geochim. Cosmochim. Acta* **73**, A851.

McDonough W. F. (2003) Compositional model for the Earth's core. In *Treatise on Geochemistry* (eds. D. H. Heinrich (Editors-in-Chief) and K. T. Karl). Pergamon, Oxford. pp. 547–568.

McDonough W. F. and Sun S. S. (1995) The composition of the earth. *Chem. Geol.* **120**, 223–253.

Medard E., McCammon C. A., Barr J. A. and Grove T. L. (2008) Oxygen fugacity, temperature reproducibility, and H_2O contents of nominally anhydrous piston-cylinder experiments using graphite capsules. *Am. Mineral.* **93**, 1838–1844.

O'Neill H. S. (1987) Quartz–fayalite–iron and quartz–fayalite–magnetite equilibria and the free-energy of formation of fayalite (Fe_2SiO_4) and magnetite (Fe_3O_4). *Am. Mineral.* **72**, 67–75.

Pertermann M. and Hirschmann M. M. (2002) Trace-element partitioning between vacancy-rich eclogitic clinopyroxene and silicate melt. *Am. Mineral.* **87**, 1365–1376.

Pertermann M. and Hirschmann M. M. (2003) Anhydrous partial melting experiments on MORB-like eclogite: phase relations, phase compositions and mineral-melt partitioning of major elements at 2–3 GPa. *J. Petrol.* **44**, 2173–2201.

Pertermann M., Hirschmann M. M., Hametner K., Gunther D. and Schmidt M. W. (2004) Experimental determination of trace element partitioning between garnet and silica-rich liquid during anhydrous partial melting of MORB-like eclogite. *Geochem. Geophys. Geosyst.* **5**.

Pilet S., Hernandez J., Sylvester P. and Poujol M. (2005) The metasomatic alternative for ocean island basalt chemical heterogeneity. *Earth Planet. Sci. Lett.* **236**, 148–166.

Putirka K., Johnson M., Kinzler R., Longhi J. and Walker D. (1996) Thermobarometry of mafic igneous rocks based on clinopyroxene–liquid equilibria, 0–30 kbar. *Contrib. Miner. Petrol.* **123**, 92–108.

Qin L. P. and Humayun M. (2008) The Fe/Mn ratio in MORB and OIB determined by ICP-MS. *Geochim. Cosmochim. Acta* **72**, 1660–1677.

Ray G. L., Shimizu N. and Hart S. R. (1983) An ion microprobe study of the partitioning of trace-elements between clinopyroxene and liquid in the system diopside–albite–anorthite. *Geochim. Cosmochim. Acta* **47**, 2131–2140.

Rhodes J. M. and Vollinger M. J. (2005) Ferric/ferrous ratios in 1984 Mauna Loa lavas: a contribution to understanding the oxidation state of Hawaiian magmas. *Contrib. Miner. Petrol.* **149**, 666–674.

Robinson J. A. C. and Wood B. J. (1998) The depth of the spinel to garnet transition at the peridotite solidus. *Earth Planet. Sci. Lett.* **164**, 277–284.

Ruzicka A., Snyder G. A. and Taylor L. A. (2001) Comparative geochemistry of basalts from the Moon, Earth, HED asteroid, and Mars: implications for the origin of the Moon. *Geochim. Cosmochim. Acta* **65**, 979–997.

Shannon R. D. (1976) Revised effective ionic-radii and systematic studies of interatomic distances in halides and chalcogenides. *Acta Crystallogr. Sec. A* **32**, 751–767.

Shervais J. W. (1982) Ti–V plots and the petrogenesis of modern and ophiolitic lavas. *Earth Planet. Sci. Lett.* **59**, 101–118.

Shimizu N. and Kushiro I. (1975) Partitioning of rare-Earth elements between garnet and liquid at high-pressures – preliminary experiments. *Geophys. Res. Lett.* **2**, 413–416.

Sobolev A. V., Hofmann A. W., Sobolev S. V. and Nikogosian I. K. (2005) An olivine-free mantle source of Hawaiian shield basalts. *Nature* **434**, 590–597.

Sobolev A. V., Hofmann A. W., Kuzmin D. V., Yaxley G. M., Arndt N. T., Chung S. L., Danyushevsky L. V., Elliott T., Frey F. A., Garcia M. O., Gurenko A. A., Kamenetsky V. S., Kerr A. C., Krivolutskaya N. A., Matvienkov V. V., Nikogosian I. K., Rocholl A., Sigurdsson I. A., Sushchevskaya N. M. and Teklay M. (2007) The amount of recycled crust in sources of mantle-derived melts. *Science* **316**, 412–417.

Suzuki T. and Akaogi M. (1995) Element partitioning between olivine and silicate melt under high-pressure. *Phys. Chem. Miner.* **22**, 411–418.

Takahashi E. (1986) Melting of a dry peridotite KLB-1 up to 14 GPa – implications on the origin of peridotitic upper mantle. *J. Geophys. Res. Solid Earth Planets* **91**, 9367–9382.

Takahashi E., Shimazaki T., Tsuzaki Y. and Yoshida H. (1993) Melting study of a peridotite KLB-1 to 6.5 GPa, and the origin of basaltic magmas. *Philos. Trans. Phys. Sci. Eng.* **342**, 105–120.

Taura H., Yurimoto H., Kurita K. and Sueno S. (1998) Pressure dependence on partition coefficients for trace elements between olivine and the coexisting melts. *Phys. Chem. Miner.* **25**, 469–484.

Toplis M. J. (2005) The thermodynamics of iron and magnesium partitioning between olivine and liquid: criteria for assessing and predicting equilibrium in natural and experimental systems. *Contrib. Miner. Petrol.* **149**, 22–39.

van Kan Parker M., Liebscher A., Frei D., van Sijl J., van Westrenen W., Blundy J. and Franz G. (2010) Experimental and computational study of trace element distribution between orthopyroxene and anhydrous silicate melt: substitution mechanisms and the effect of iron. *Contrib. Miner. Petrol.* **159**, 459–473.

van Westrenen W., Blundy J. and Wood B. (1999) Crystal-chemical controls on trace element partitioning between garnet and anhydrous silicate melt. *Am. Mineral.* **84**, 838–847.

Walter M. J. (1998) Melting of garnet peridotite and the origin of komatiite and depleted lithosphere. *J. Petrol.* **39**, 29–60.

Weaver B. L. (1991) The origin of ocean island basalt end-member compositions – trace-element and isotopic constraints. *Earth Planet. Sci. Lett.* **104**, 381–397.

Wilson S. A. (1997a) The collection, preparation, and testing of USGS reference material BCR-2, Columbia River, Basalt. In (ed. U. S. G. Survey). Available from: <http://crustal.usgs.gov/geochemical_reference_standards/basaltbcr2.html>.

Wilson S. A. (1997b) Data compilation for USGS reference material BHVO-2, Hawaiian Basalt. in: (ed. U. S. G. Survey). Available from: <http://crustal.usgs.gov/geochemical_reference_standards/basaltbhvo2.html>.

Xirouchakis D., Hirschmann M. M. and Simpson J. A. (2001) The effect of titanium on the silica content and on mineral–liquid partitioning of mantle-equilibrated melts. *Geochim. Cosmochim. Acta* **65**, 2201–2217.

Yaxley G. M. and Green D. H. (1998) Reactions between eclogite and peridotite: mantle refertilisation by subduction of oceanic crust. *Schweiz. Mineral. Petrogr. Mitt.* **78**, 243–255.

Zangana N. A., Downes H., Thirlwall M. F., Marriner G. F. and Bea F. (1999) Geochemical variation in peridotite xenoliths and their constituent clinopyroxenes from Ray Pic (French Massif Central): implications for the composition of the shallow lithospheric mantle. *Chem. Geol.* **153**, 11–35.

Zindler A. and Hart S. (1986) Chemical geodynamics. *Annu. Rev. Earth Planet. Sci.* **14**, 493–571.

Associate editor: Michael Toplis